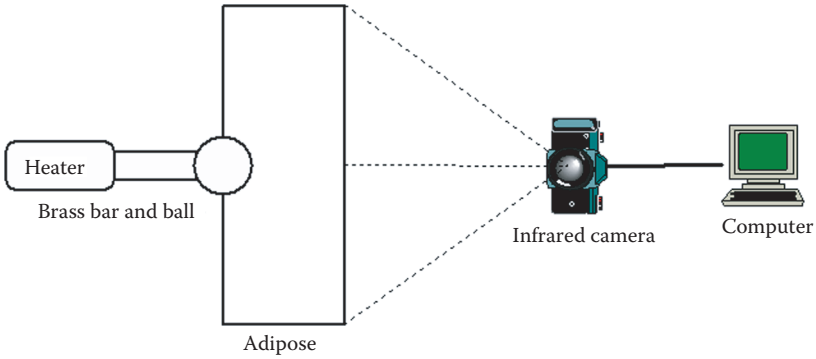

FIGURE 9.1 Illustration of the experimental setup where an internal ball heat source (e.g., brass ball) was imbedded in a piece of adipose tissue. For color figures, see www.holistichealthscience.org.

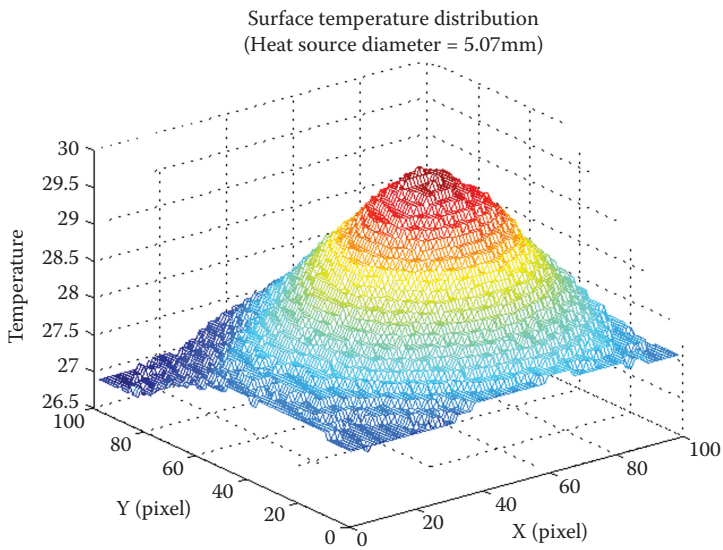

FIGURE 9.2 Illustration of the surface temperature distribution of the internal source of Figure 9.1. For color figures, see www.holistichealthscience.org.

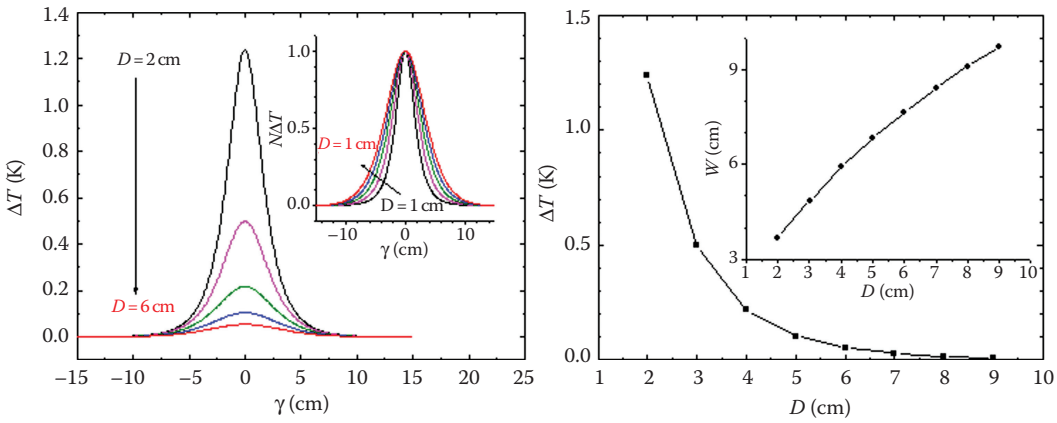

FIGURE 9.3 Left: temperature distributions on the phantom surface of the heat source. Baseline temperature was subtracted to obtain the relative temperature DT(r) and its normalized term NDT(r); r is the radius on the phantom surface away from the center of the source. Right: change of the DT(r=0) and its width W versus the source depth D. For color figures, see www.holistichealthscience.org.

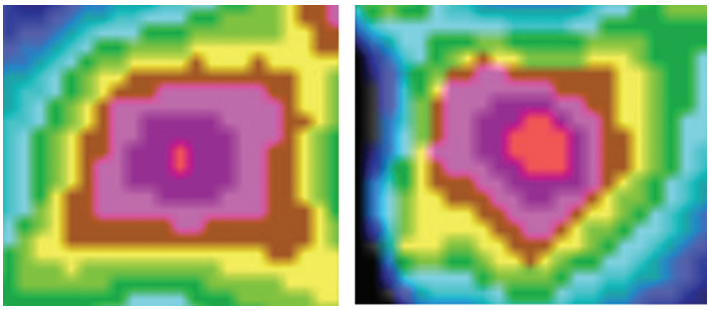

FIGURE 9.4 Illustration of the isothermal contours of the surface temperature distributions of heat sources at different depths. Left: a skin surface source with a greater distance between the isothermal contours. Right: a deep tissue source with closer distance between the isothermal contours. For color figures, see www.holistichealth-science.org.

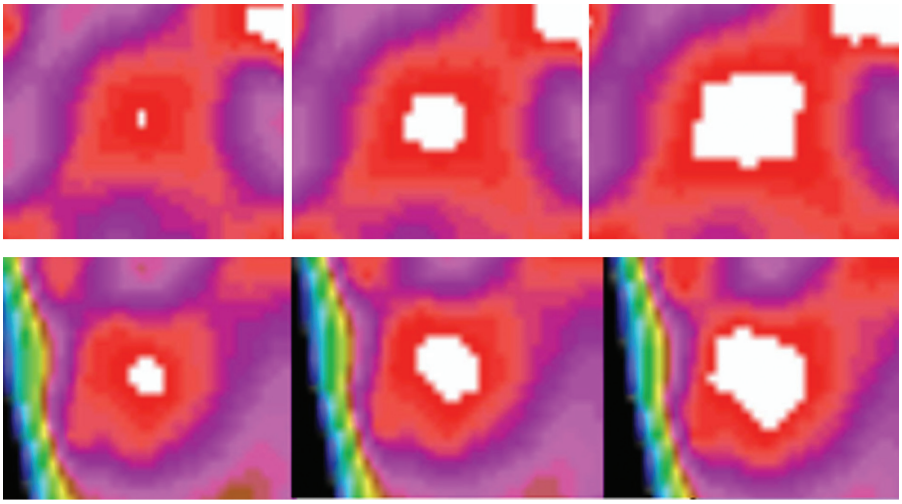

FIGURE 9.5 Illustration of the dynamic slicing technique in displaying the isothermal contours. The white area is the isothermal contour above certain temperature level corresponding to those contours shown in Figure 9.4. The temperature level is dynamically reduced every 0.05°C in a movie mode (three frames of the movie are shown here). Top: a skin surface source with greater changes between the isothermal contours. Bottom: a deep tissue source with gradual changes between the isothermal contours. For color figures, see www.holistichealthscience.org.

FIGURE 9.6 Illustration of the hardware equipment of a TTM system. For color figures, see www.holistichealth-science.org.

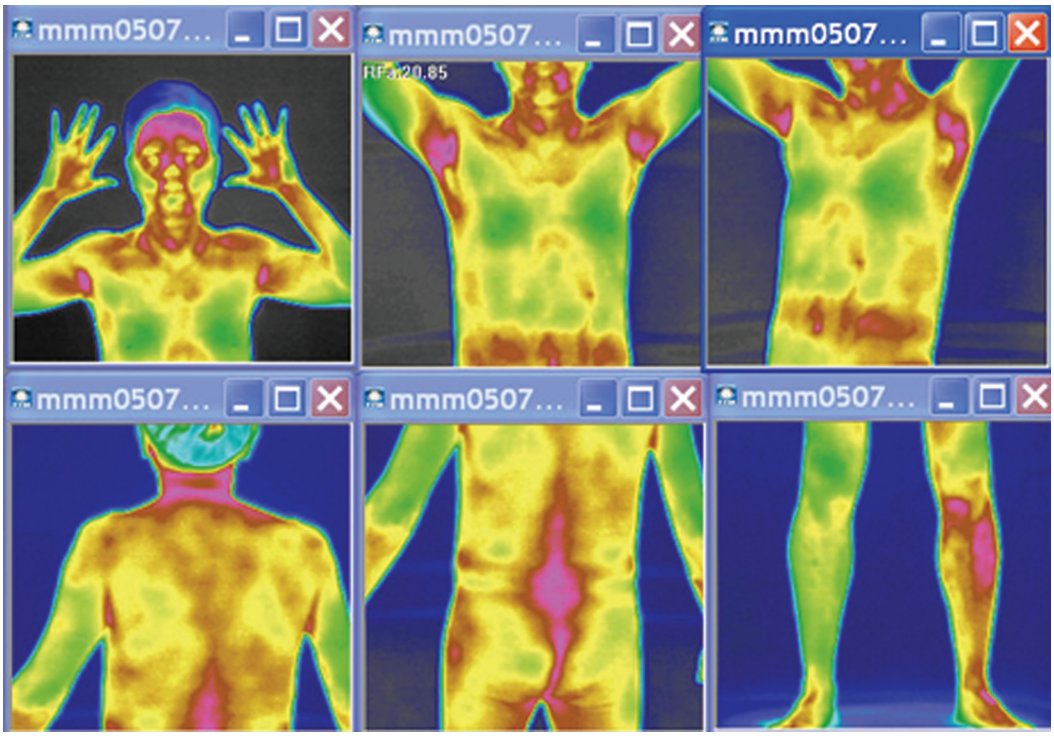

FIGURE 9.7 Typical poses used in a whole-body scan using the TTM system. For color figures, see www.holistichealthscience.org.

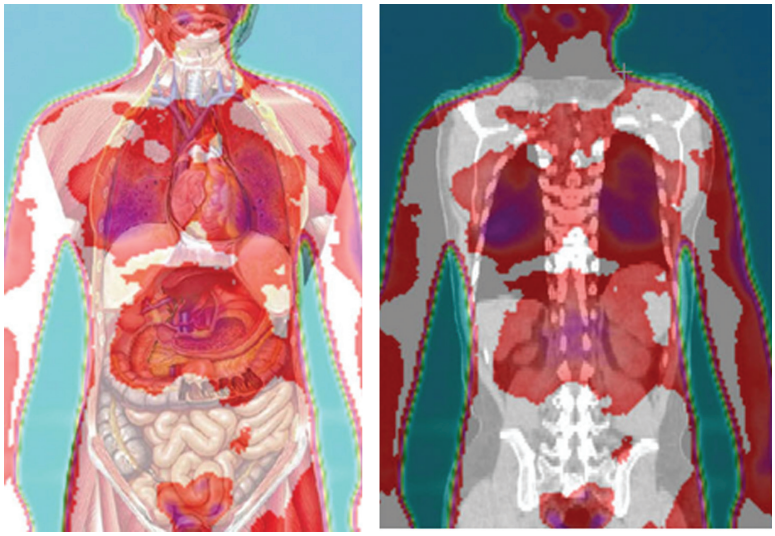

FIGURE 9.8 TTM images are fused with anatomical template (left) and reconstructed CT images of a coronal plane of the studied subject. For color figures, see www.holistichealthscience.org.

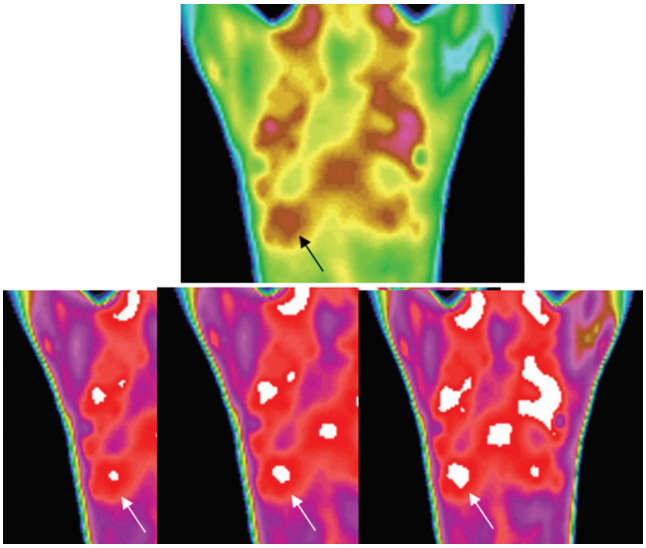

FIGURE 9.9 TTM images of a studied subject with hemangioma of the liver, shown by the arrow. Top: temperature map; bottom: dynamic slicing used in TTM and isothermal contours shown by the white areas. For color figures, see www.holistichealthscience.org.

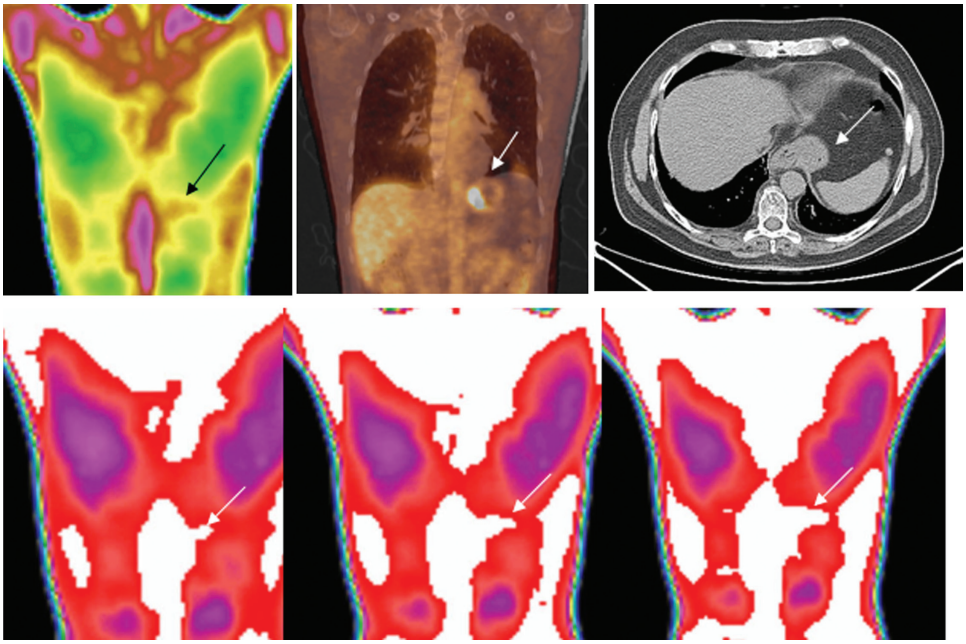

FIGURE 9.10 TTM images of a studied subject with stage III cancer of the stomach, shown by the arrow. Top: temperature map, PET/CT, and a CT axial cut; bottom: dynamic slicing used in TTM and isothermal contours shown by the white areas of the lesion.

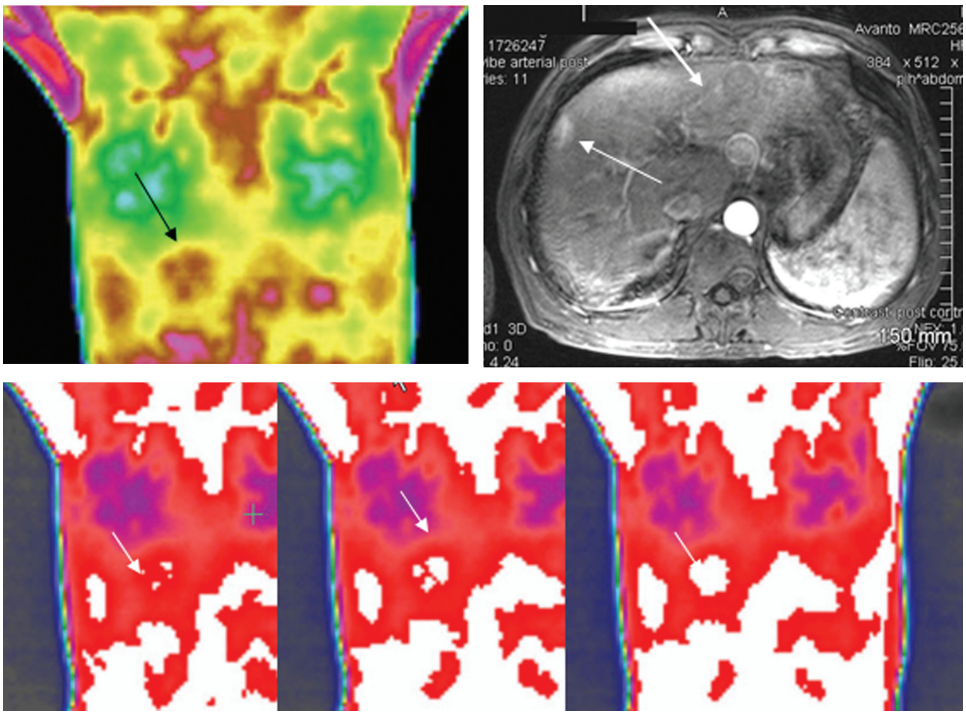

FIGURE 9.11 TTM images of a studied subject with stage IV cancer of the liver, shown by the arrows. Top: temperature map, an MRI axial cut; bottom: dynamic slicing used in TTM and isothermal contours shown by the white areas of the lesions. For color figures, see www.holistichealthscience.org.

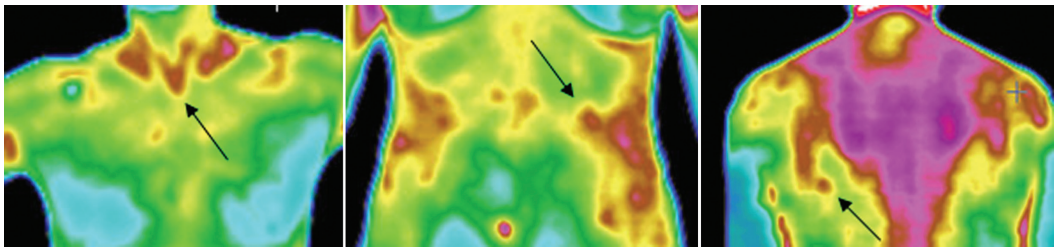

FIGURE 9.12 Thermal acupoints that are associated with stomach disorders. Left: acupoint near the superclavicular notch of the same subject of Figure 9.10. Mid and right: acupoints near the left middle abdomen and left back of another subject. For color figures, see www.holistichealthscience.org.

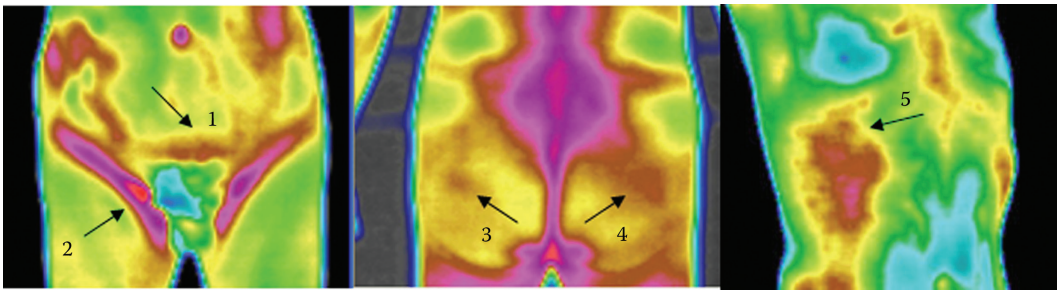

FIGURE 9.13 TTM images of a studied subject with prostate hyperplasia shown by arrow #1. Abnormal thermal activities were also observed at the pelvic lymph node area (arrow #2, back of the buttock (arrow #3, #4), and in the liver area (arrow #5). For color figures, see www.holistichealthscience.org.

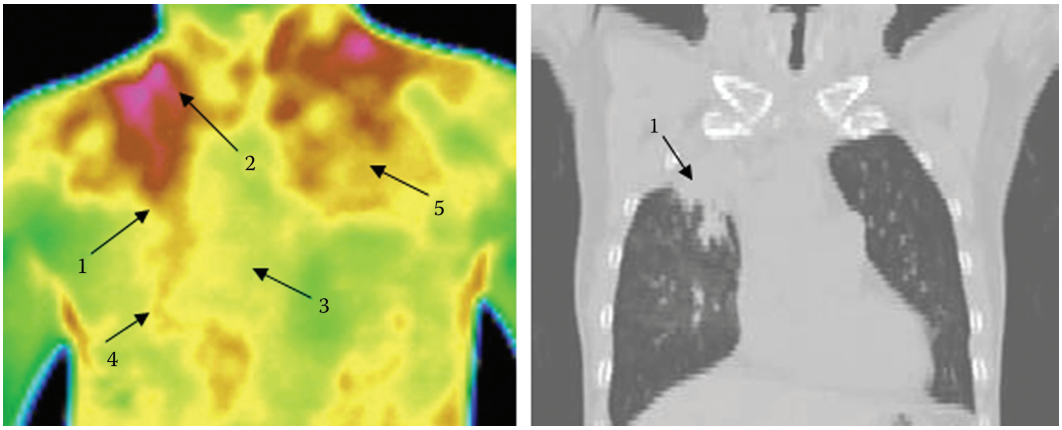

FIGURE 9.14 Images of a studied subject with cancer of the lung shown by arrow #1 on TTM image (left) and chest CT (right). Abnormal thermal activities were also observed near the right supraclavicular and mediastinum lymph node areas (arrow #2, #3, respectively), and mid right chest and upper left chest areas (arrow #4, #5, respectively). For color figures, see www.holistichealthscience.org.

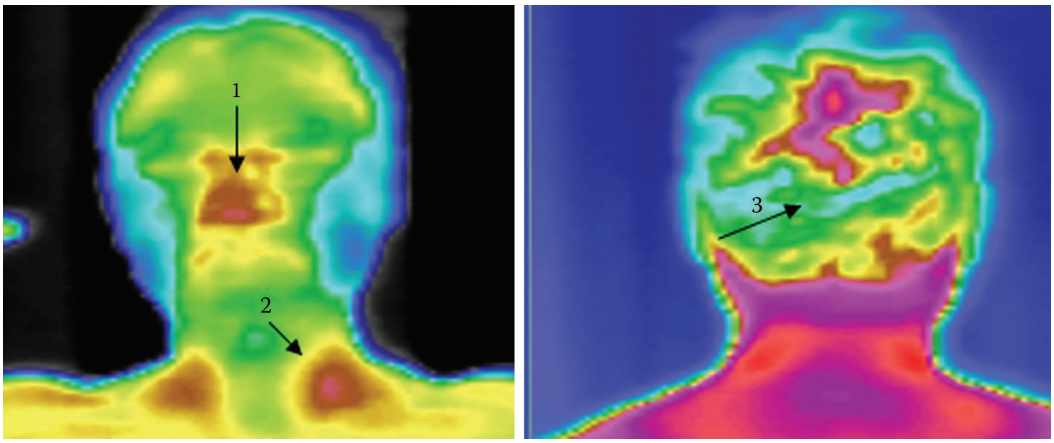

FIGURE 9.15 Images of a studied subject with nasopharynx cancer near the nose cavities (arrow #1). Abnormal thermal activities were also observed near the left neck area and supraclavicular lymph node (arrow #2) and from the back of the head (arrow #3). For color figures, see www.holistichealthscience.org.

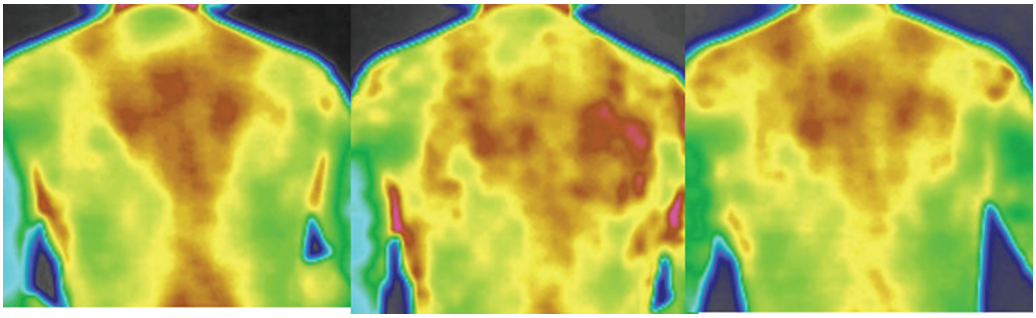

FIGURE 9.16 The effect of stress and its mitigation shown by TTM images. Left: morning condition with low mental stress; middle: evening condition with high mental stress; right: 1 h after the evening scan of the middle panel with 30 min of relaxation meditation. For color figures, see www.holistichealthscience.org.

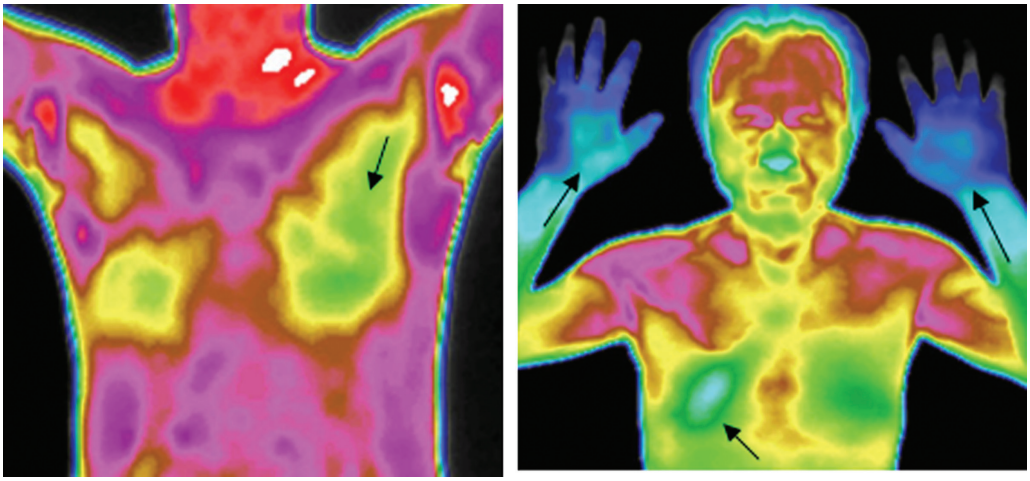

FIGURE 9.17 Left: thermal deficiency in the left chest area (shown by the arrow) associated with a subject with coronary artery disease and cardiac ischemia. Right: thermal deficiency in the right chest area and of the palms and the smaller fingers (shown by the arrows) in a subject who had chronic fatty liver and high cholesterol. High blood pressure experienced by this subject shown as thermal elevation in the head and upper shoulder area. For color figures, see www.holistichealthscience.org.

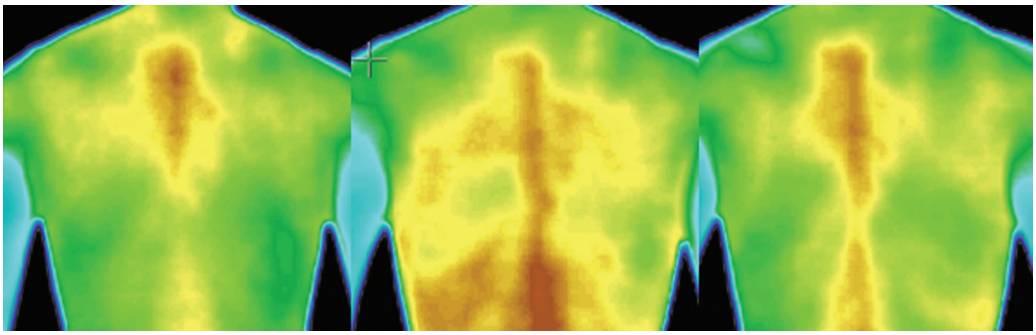

FIGURE 9.18 Thermal pattern changes of a studied subject undergoing cancer chemotherapy. Left: prior to chemotherapy; middle: post chemotherapy 2 months after the first scan; right: 1 h after the scan of the middle panel and with oral intake of a dose of herbal supplement to mitigate side effects of chemotherapy. For color figures, see www.holistichealthscience.org.

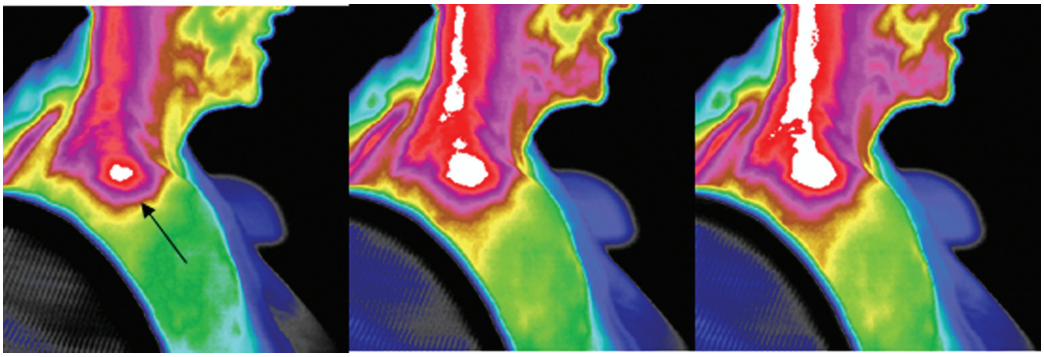

FIGURE 9.19 Thermal pattern changes of a studied subject after applying moxibustion treatment at an acupoint on the shoulder (GB21 of the gall bladder meridian, shown by the arrow). Thermal increase was seen along the side of the neck along this meridian after 5, 10, and 15 min (left, middle, and right panels, respectively) after the treatment and was in agreement with the same feeling of warming up of the neck experienced by the subject. For color figures, see www.holistichealthscience.org.

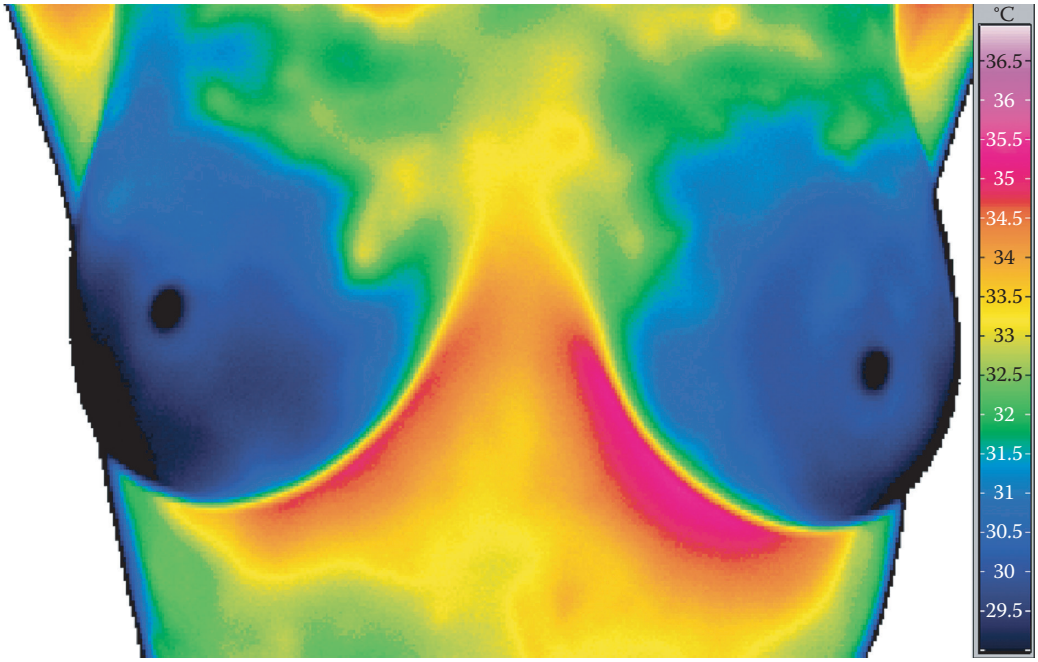

FIGURE 12.1 Normal MammoVision result of a 29-year-old healthy woman: symmetrically cool, no visible vessels, no hot spots, nipple and areola cold, contour without bulge or edge sign.

FIGURE 12.2 Medically approved infrared camera Jenoptik (formerly Carl Zeiss Jena) VarioCam Head.

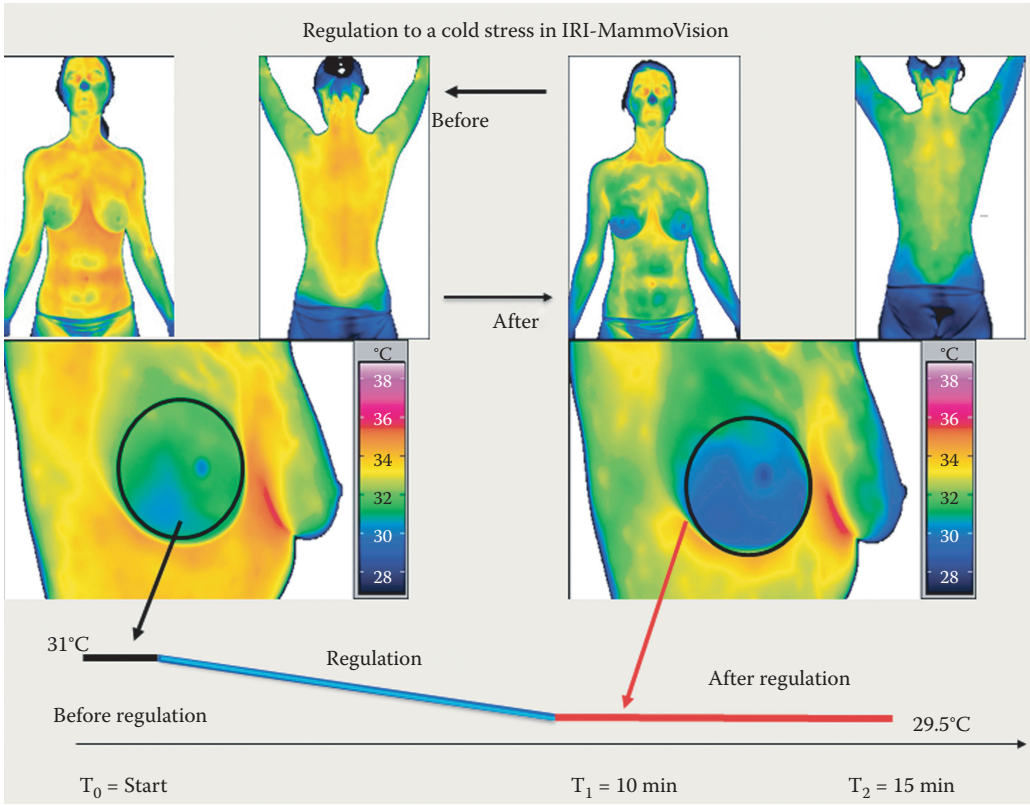

FIGURE 12.3 Principles of IRI (Infrared Regulation Imaging) and MammoVision.

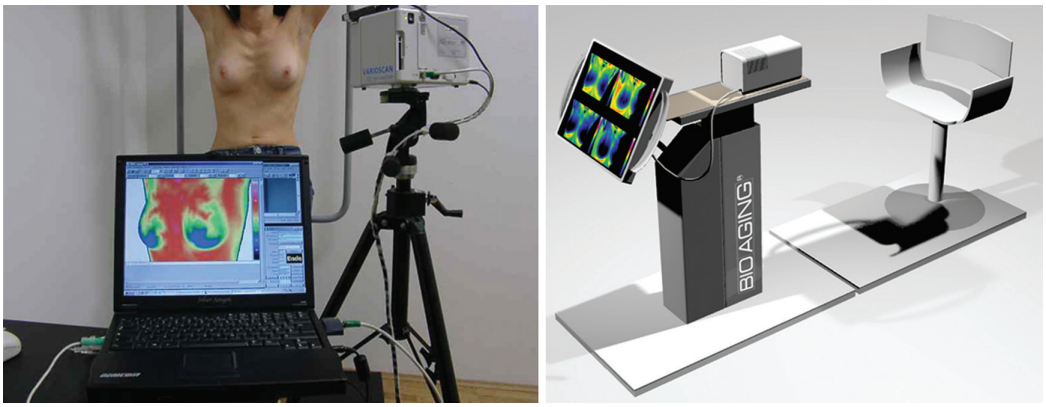

FIGURE 12.4 Early prototype of MammoVision (2000, left) and recent MammoVision device (bioaging Stuttgart, Germany, right).

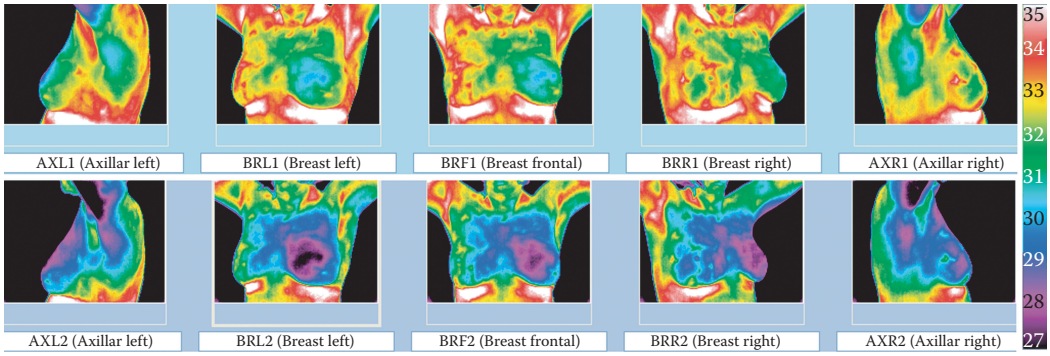

FIGURE 12.5 Measurement views of MammoVision: upper row before cold stimulus, lower row after cold stimulus and cooling down.

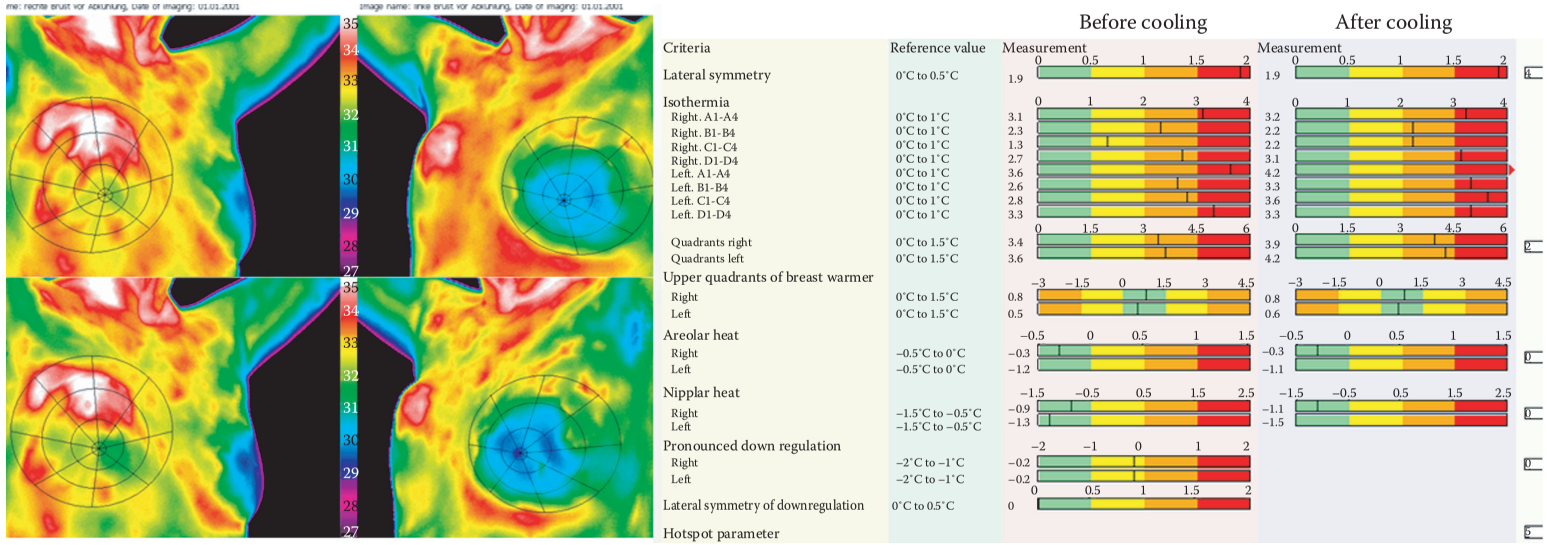

FIGURE 12.6 Positioning of the evaluation grid in MammoVision (left): upper row before, lower row after cold stimulus and cooling (woman with hot cancer in the right breast); MammoVision results in an evaluation graph (right).

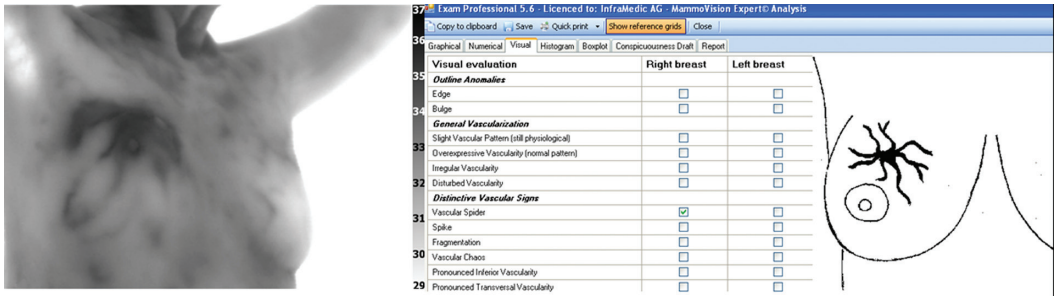

FIGURE 12.7 Grayscale masked MammoVision image for vascular description (left); MammoVision vascular description form (right).

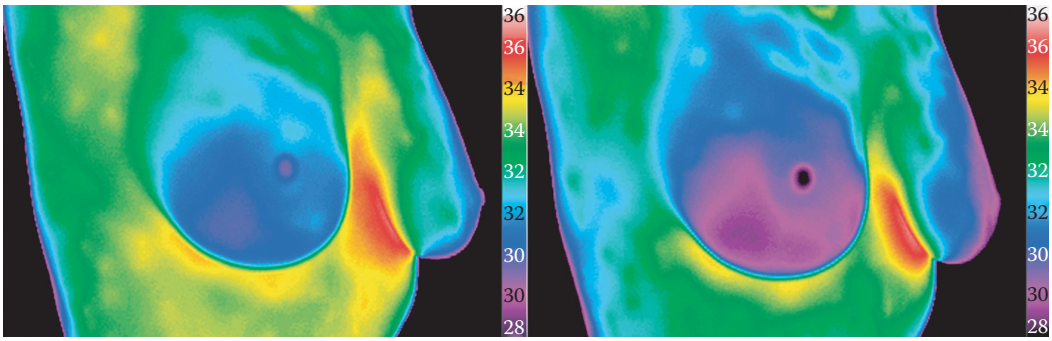

FIGURE 12.8 BIRAS I example; 29-year-old woman, left picture before cold stimulus, right picture after cold stimulus and cooling down; no clinical signs of breast disorder; in MammoVision very homogeneous, symmetrical thermal patterns, no vessels visible.

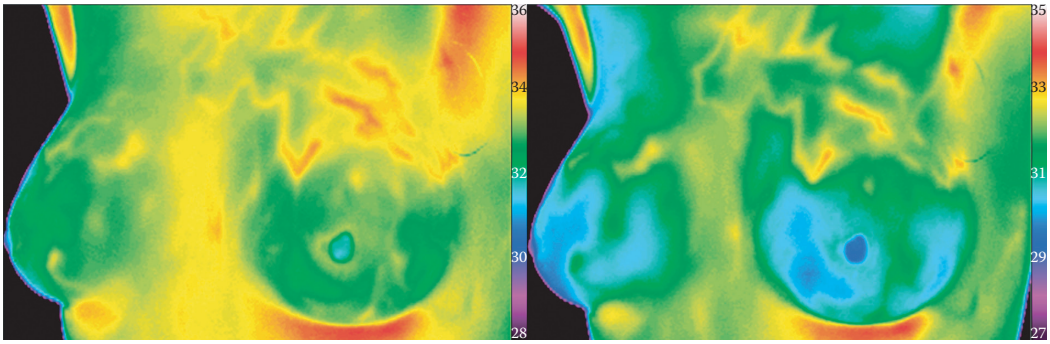

FIGURE 12.9 BIRAS II example; 42-year-old woman, left picture before cold stimulus, right picture after cold stimulus and cooling down; mastopathia, no other breast disease; MammoVision: symmetrical thermal pattern, areola and nipple cool, sufficient thermal down cold stimulus, small vessels that mostly disappear to be visible after cooling.

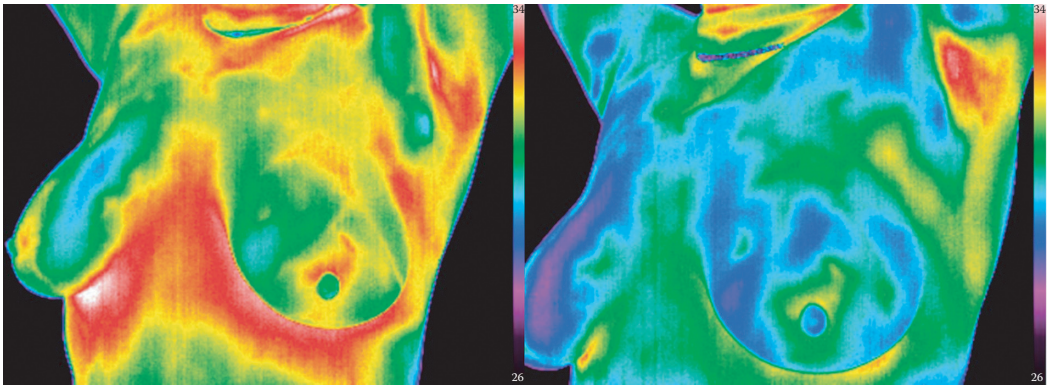

FIGURE 12.10 BIRAS III example; 43-year-old woman, left picture before cold stimulus, right picture after cold stimulus and cooling down; mastopathia, palpable nodules. MammoVision: suspicious result, areolar heat both sides, intensive down cold stimulus.

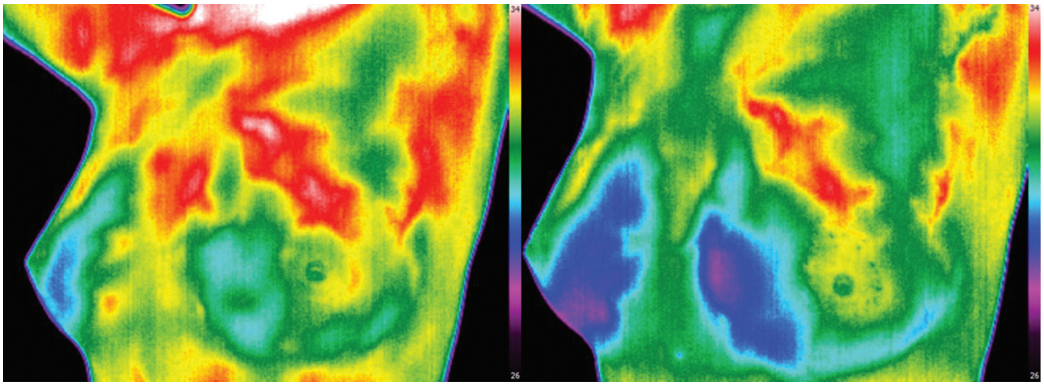

FIGURE 12.11 BIRAS IV example; 55 year old woman, left picture before cold stimulus, right picture after cold stimulus and cooling down; palpable lump in the left breast, questionable palpable axillary lymph nodes; MammoVision: very suspicious, highly asymmetrical, insufficient down cold stimulus, inflammatorious area above left areola; persisting heat even after cooling; biopsy: invasive ductal carcinoma pT2 pN1, G3, ER +, PR +, HER –.

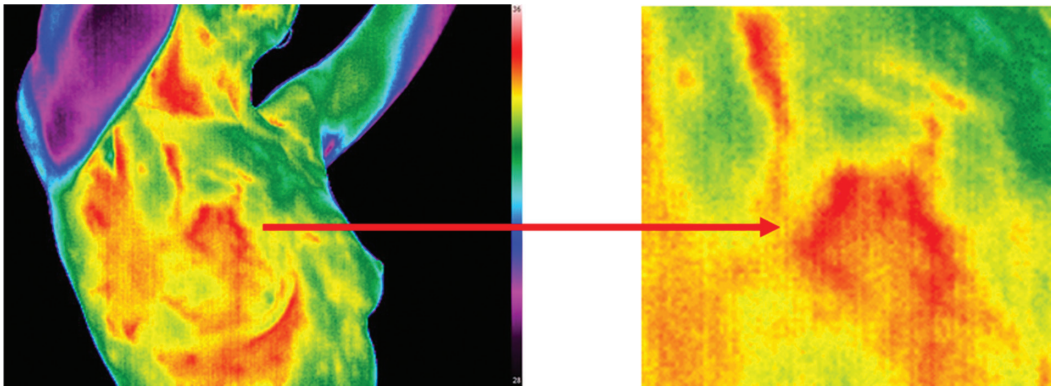

FIGURE 12.12 BIRAS V example; MammoVision very suspicious: extreme asymmetry, right breast heated intensively, absolute pathological vessel (circular structure with vascular spider aspects); biopsy: invasive ductal carcinoma; pT2 pN1, G3, ER +, PR +, HER +.

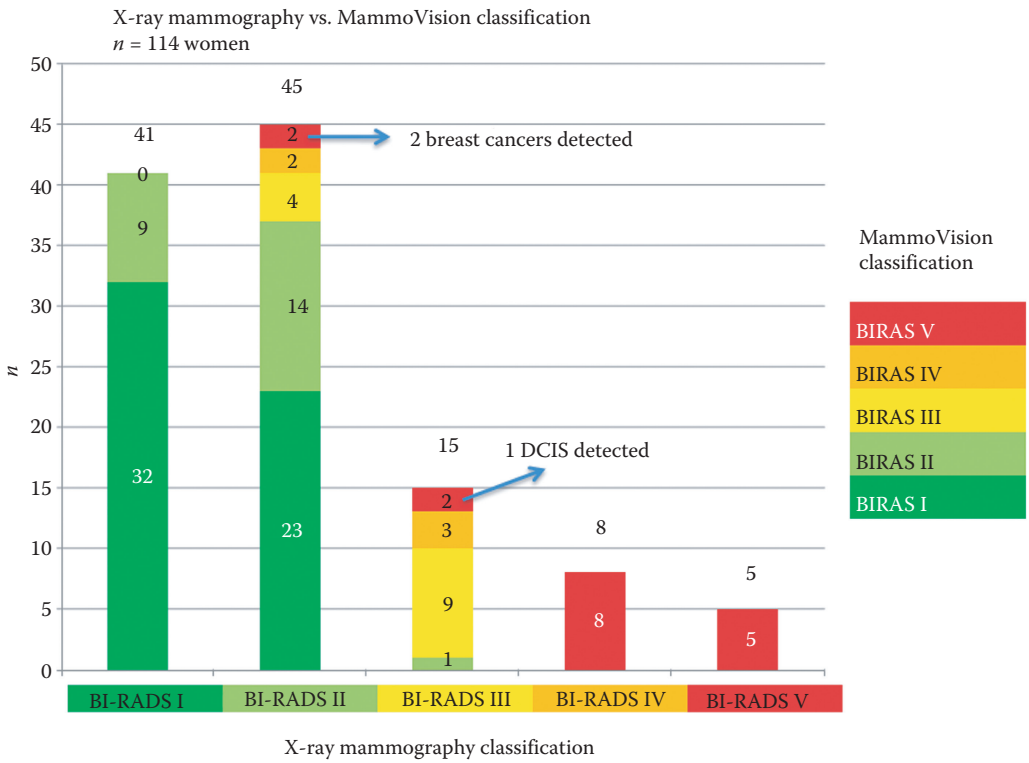

FIGURE 12.13 Comparison of x-ray mammography classification (BI-RADS I to V) versus MammoVision classification (BIRAS I to V).

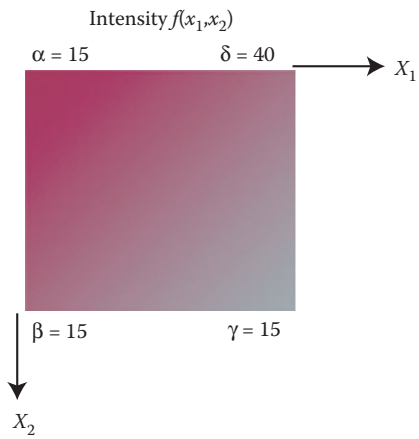

FIGURE 14.3 An example of interpolated image ($f(x_1,x_2)$) gray(light) indicates high intensity and red(dark) indicates low intensity.

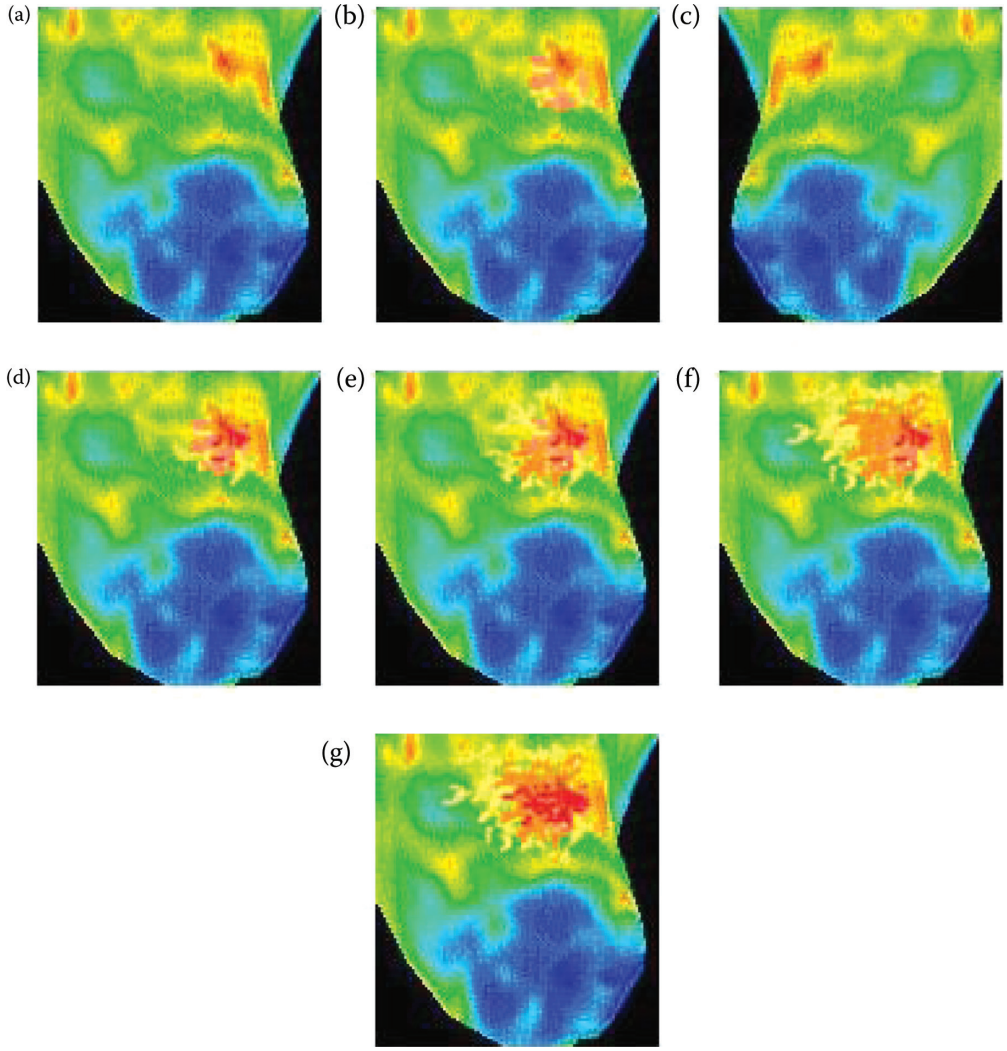

FIGURE 14.7 One image from each group. (a) Real right breast, (b) simulated left breast, (c) simulated left breast with small changes with respect to b, (d) simulated left breast with small changes with respect to c, (e) simulated left breast with small changes with respect to d, (f) simulated left breast with small changes with respect to e, (g) simulated left breast with small changes with respect to f.

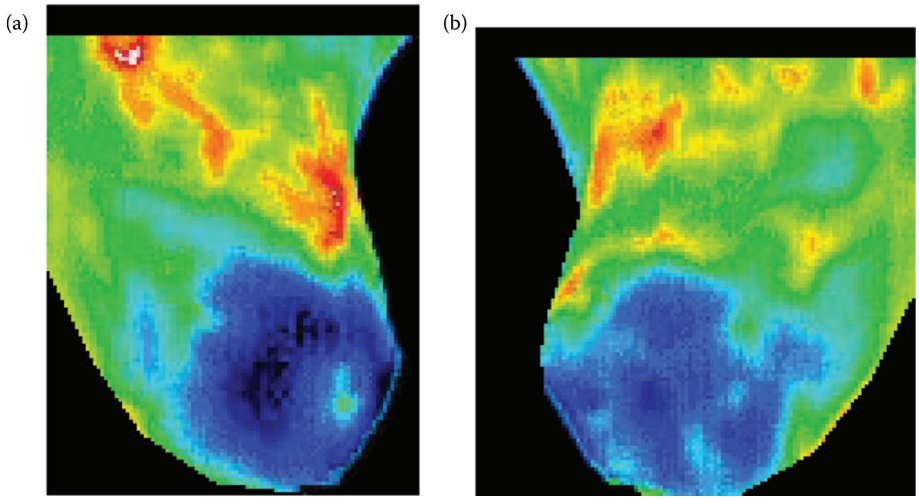

FIGURE 14.8 Original images (a) Left breast, (b) right breast.

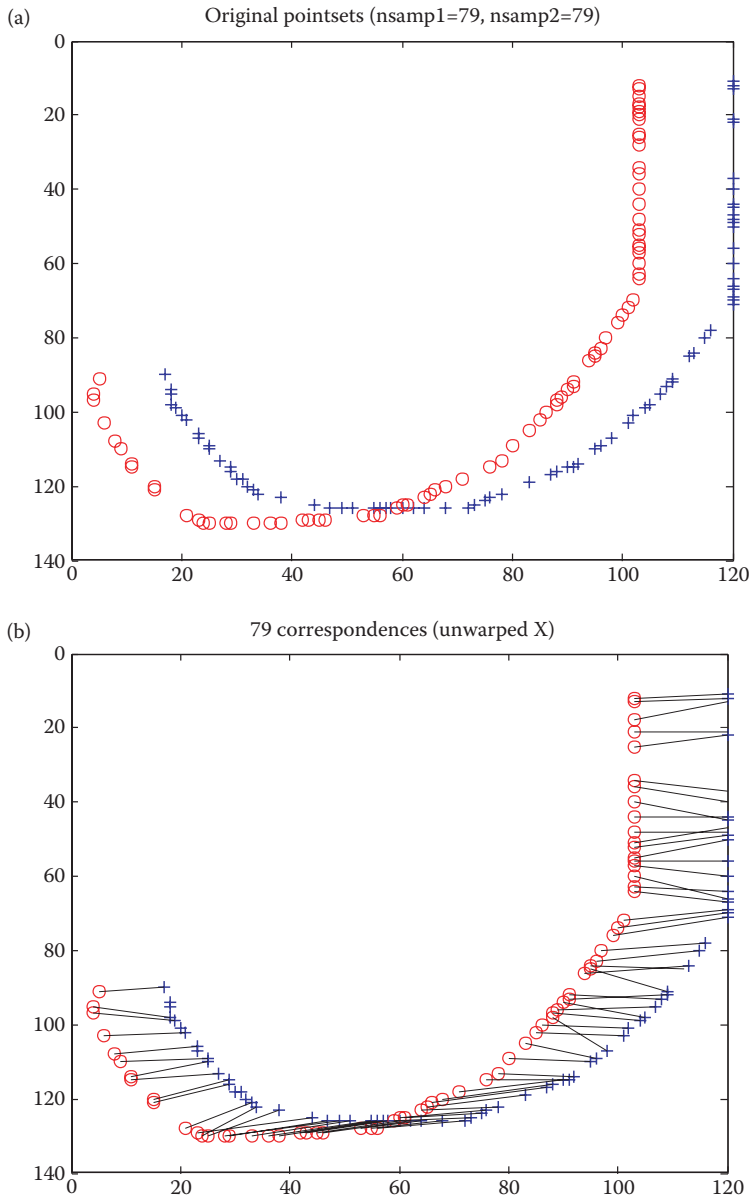

FIGURE 14.9 (a) Boundary samples of right breast (+ in blue), boundary samples of left breast (o in red) and (b) unwarped boundaries.

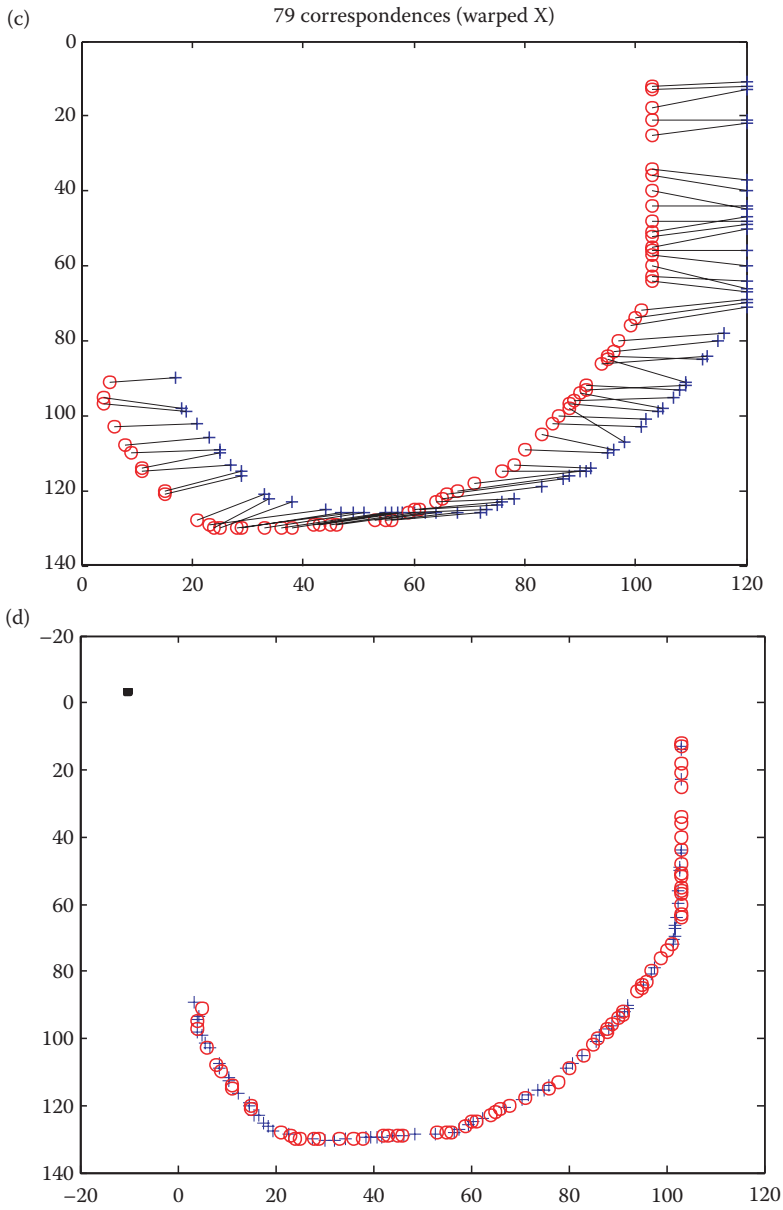

FIGURE 14.9 (continued) (c) Warped boundaries and (d) boundaries of the two breasts after employing the mapping function.

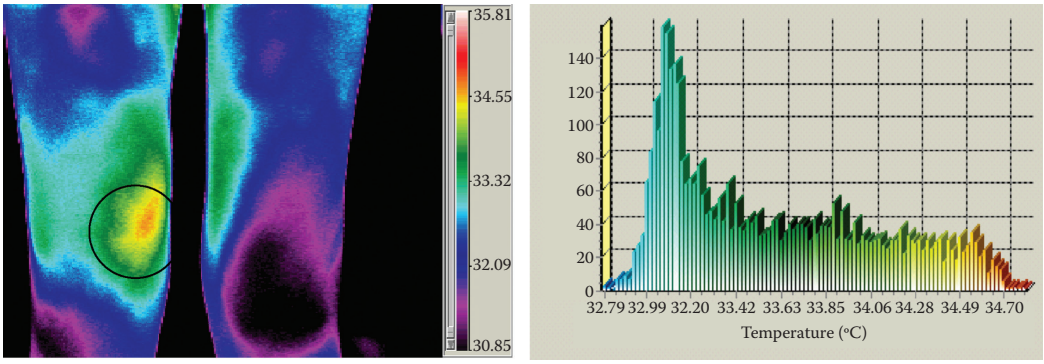

FIGURE 15.1 Thermal image and its histogram.

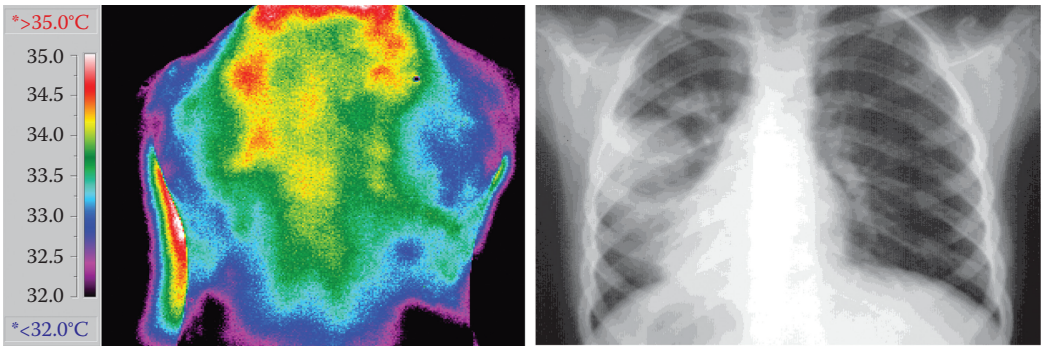

FIGURE 15.2 Thermal and x-ray images of pneumonia with asymmetric distribution of temperature.

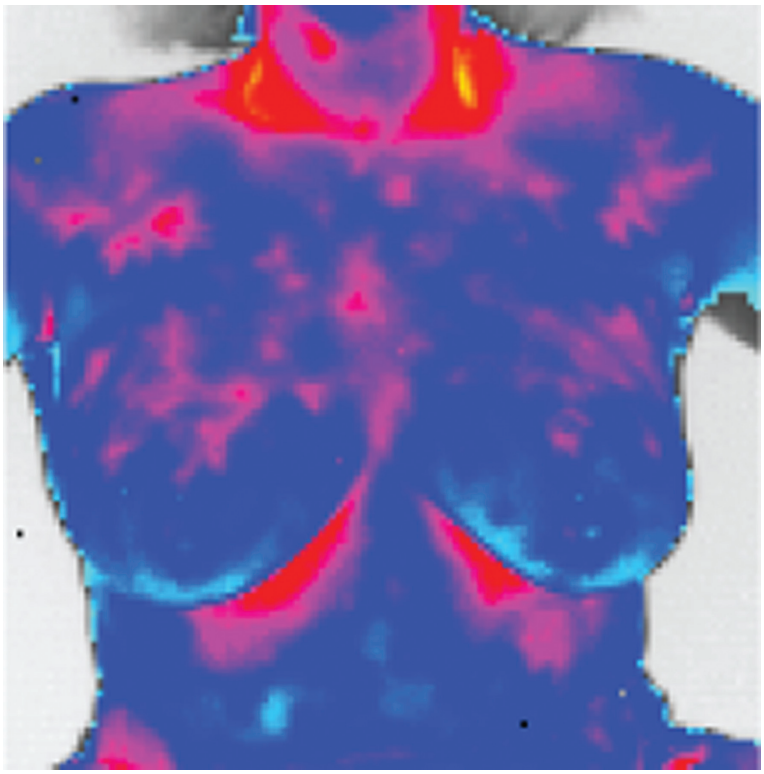

FIGURE 15.3 Thermal image of the healthy breast.

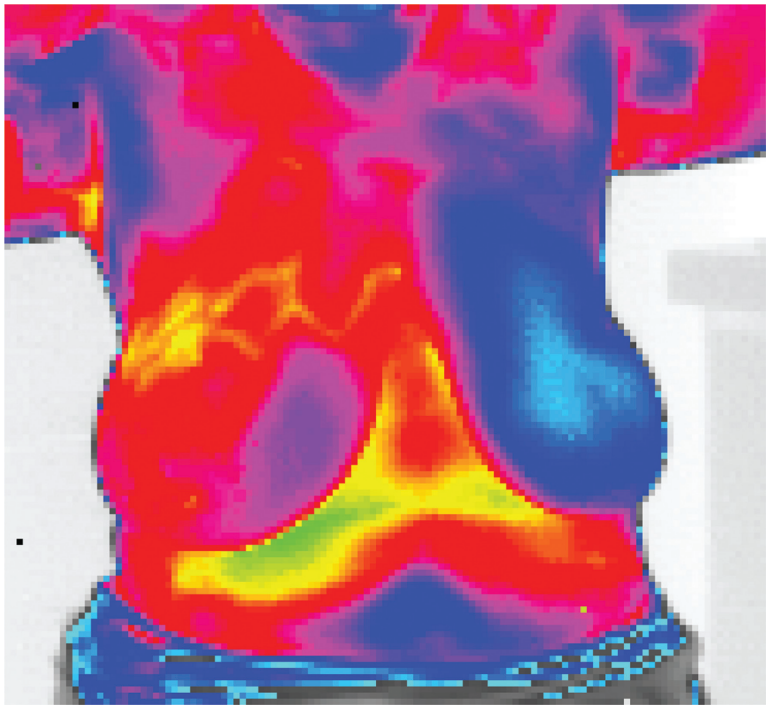

FIGURE 15.4 Thermal image of the breast with malignant tumor (left side of the image).

6	7	8
5	*	1
4	3	2

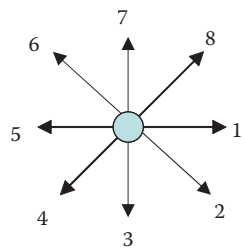

FIGURE 15.7 Eight neighboring pixels in four direct horizontal, vertical, diagonal, and antidiagonal.

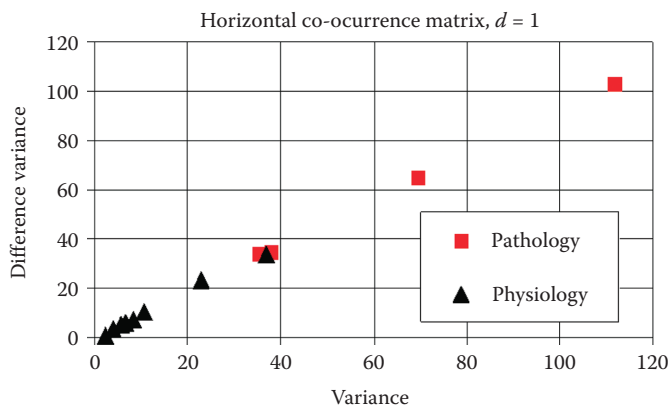

FIGURE 15.9 Difference variance versus variance obtained from co-occurrence matrix for horizontal direction.

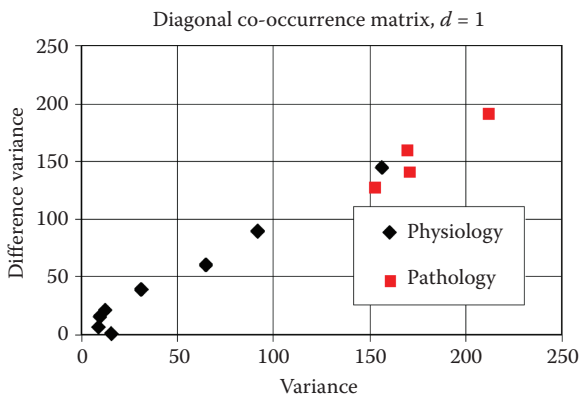

FIGURE 15.10 Difference variance versus variance obtained from co-occurrence matrix for diagonal direction.

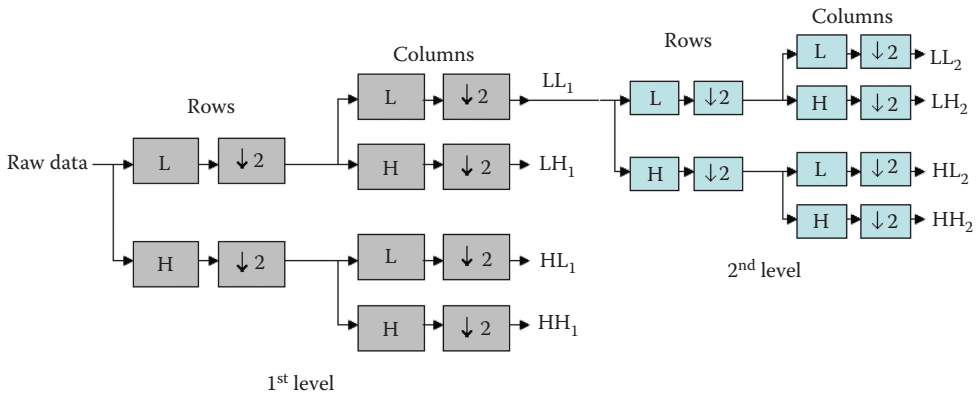

FIGURE 15.11 2D wavelet transform concept.

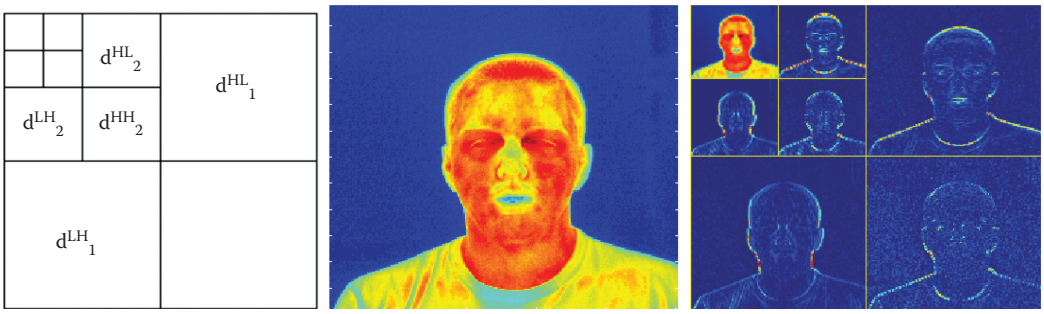

FIGURE 15.12 Typical result of 2D wavelet filtering, images' map, original and filtered images.

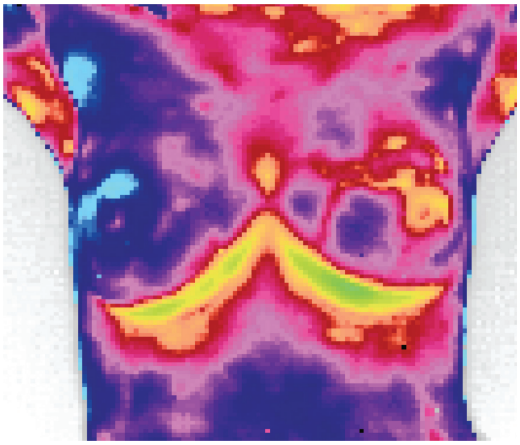

FIGURE 15.13 Example of thermal image showing the tumor (left breast).

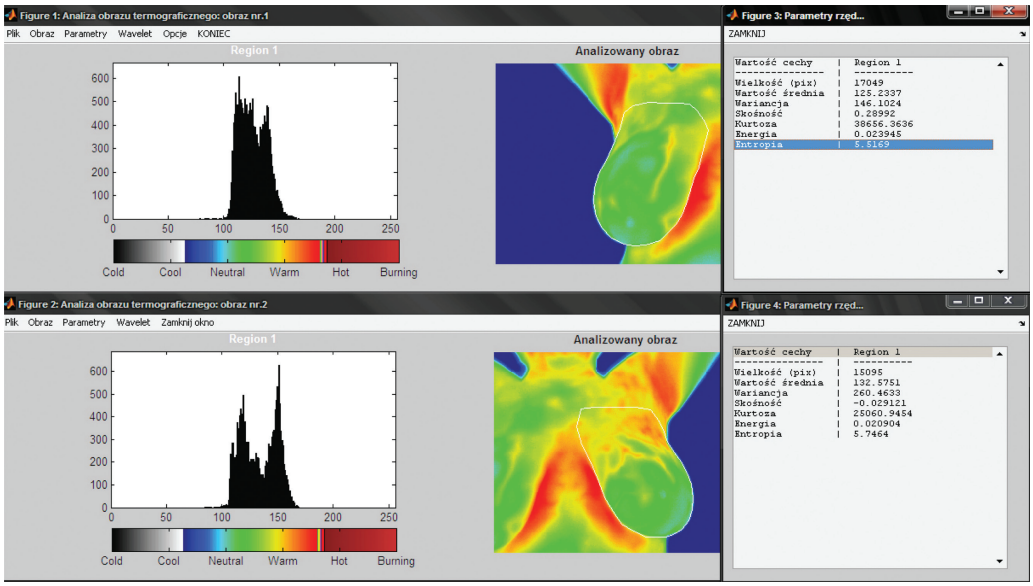

FIGURE 15.17 Application window with selected region and displayed the first-order features values.

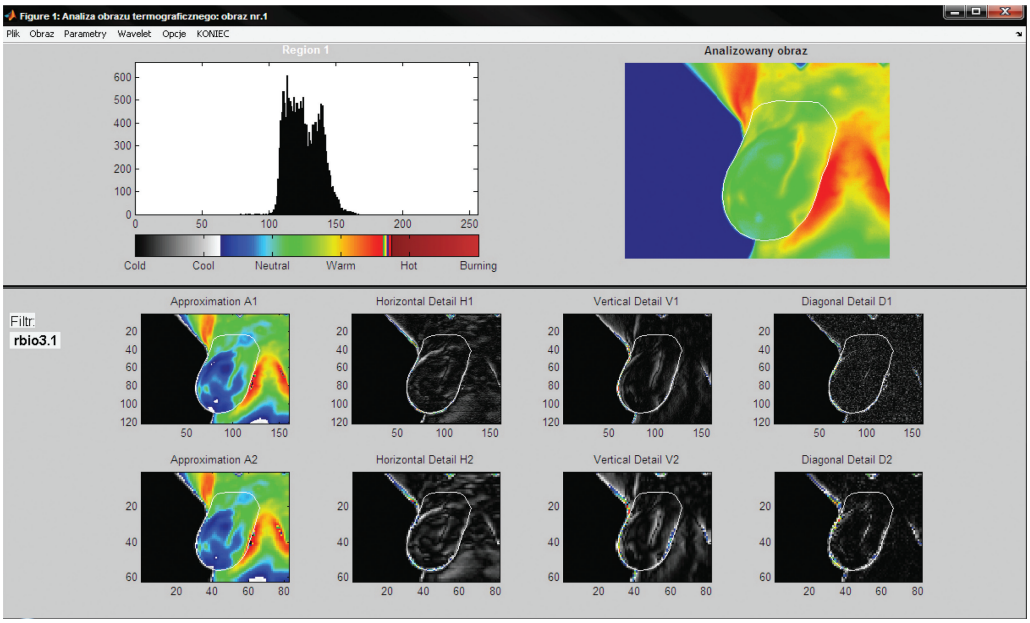

FIGURE 15.18 Results after wavelet transform for first and second filtering steps.

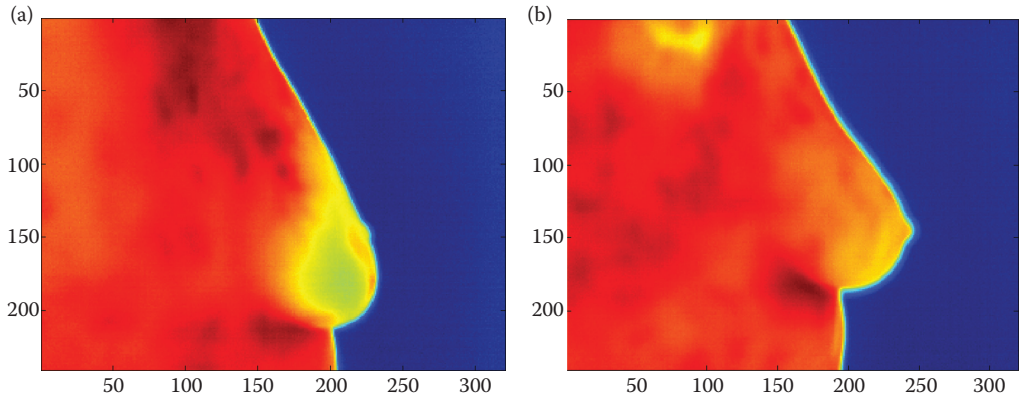

FIGURE 15.19 Exemplary side thermal images of breasts (a) with (b) without pathological change.

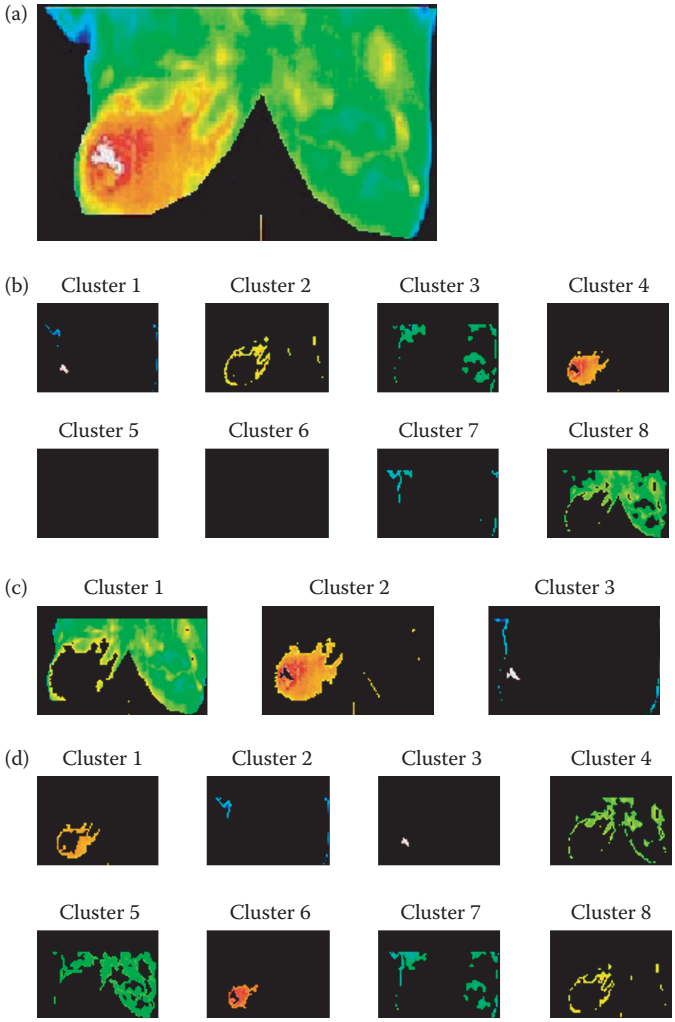

FIGURE 16.1 Inflammatory cancer case. (a) Original image (inflammatory cancer case). (b) Color segmentation by K means; two empty clusters (inflammatory cancer case). (c) Color segmentation by mean shift with $h = 35$. (d) Color segmentation by fuzzy C means.

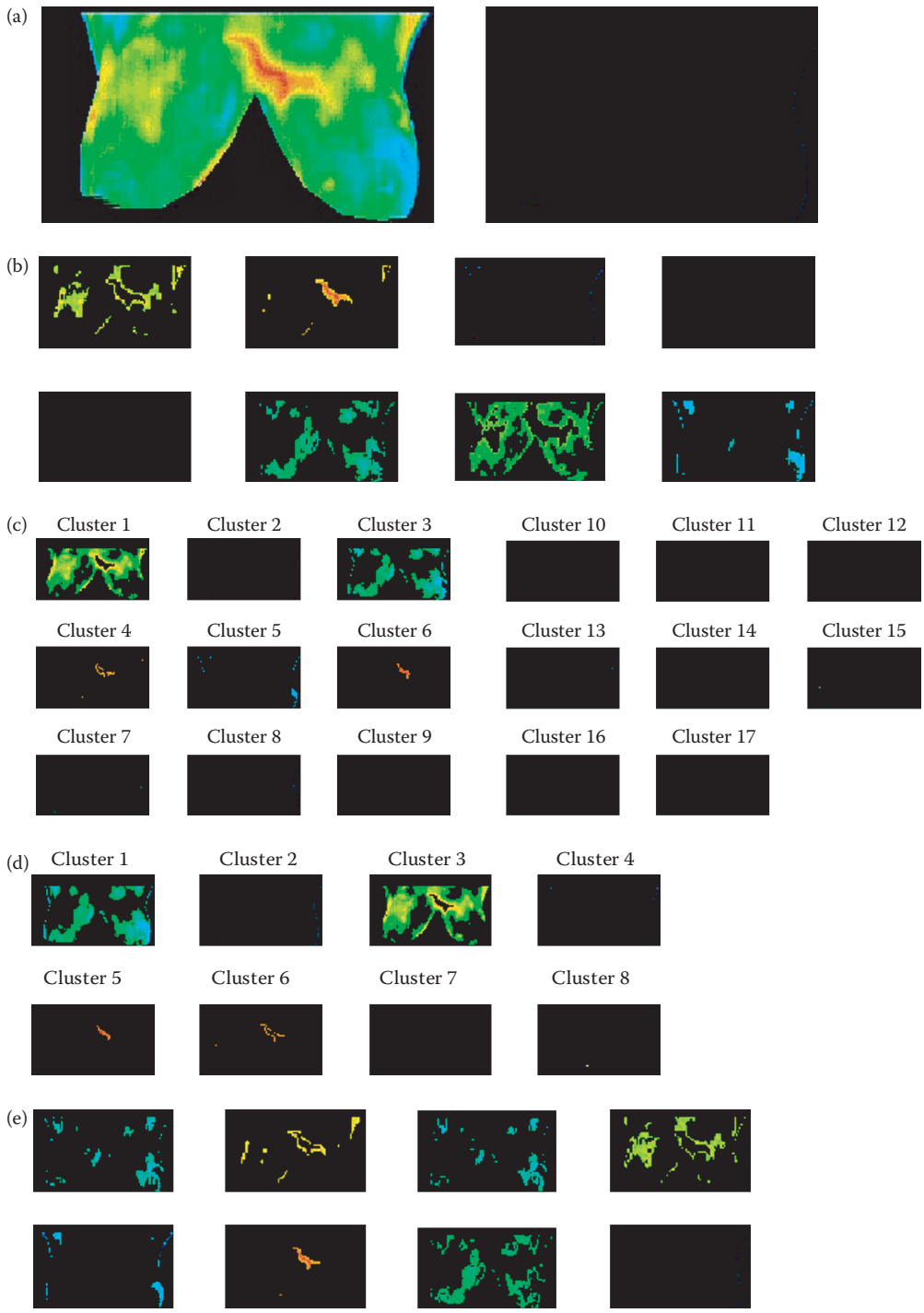

FIGURE 16.2 Normal case. (a) Original image (normal case). (b) Color segmentation by K means (three empty clusters). (c) Color segmentation by mean shift with $h = 12$ (11 empty clusters). (d) Color segmentation by mean shift with $h = 15$ (4 empty clusters). (e) Color segmentation by fuzzy C means.

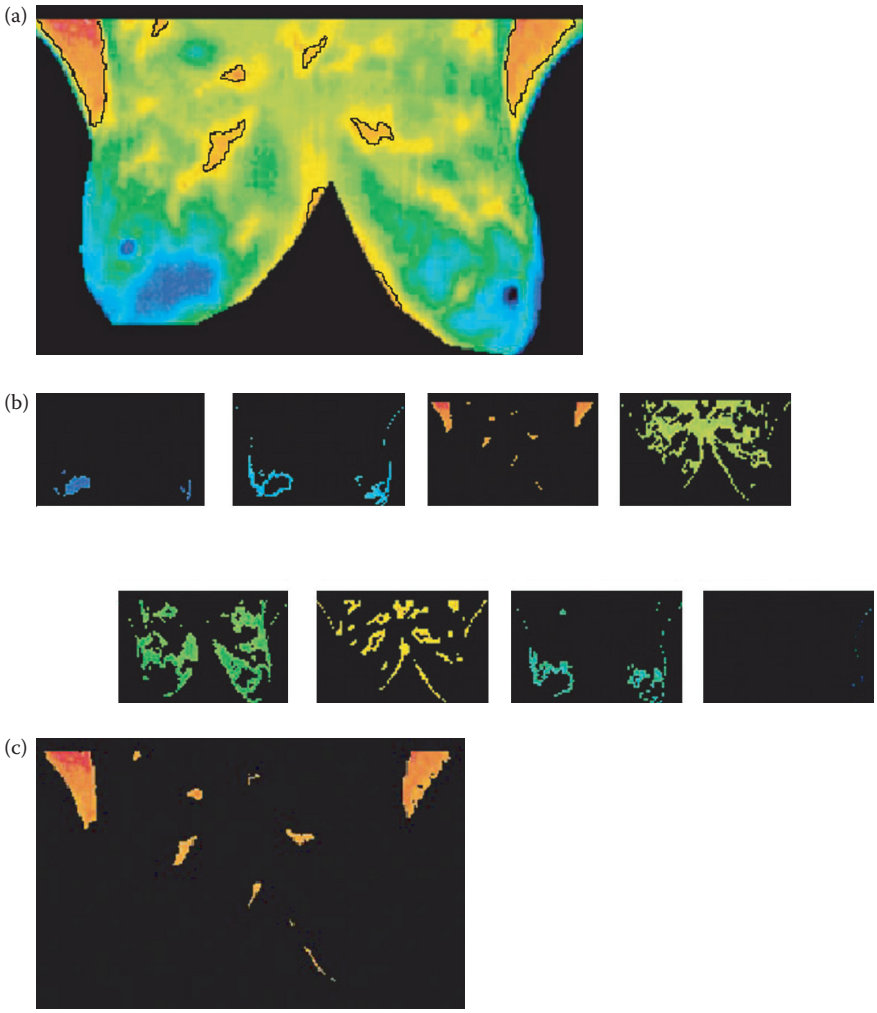

FIGURE 16.5 (a) Benign case 1 (B1). (b) Segmentation of (a) by fuzzy C mean. (c) The first hottest regions of B1.

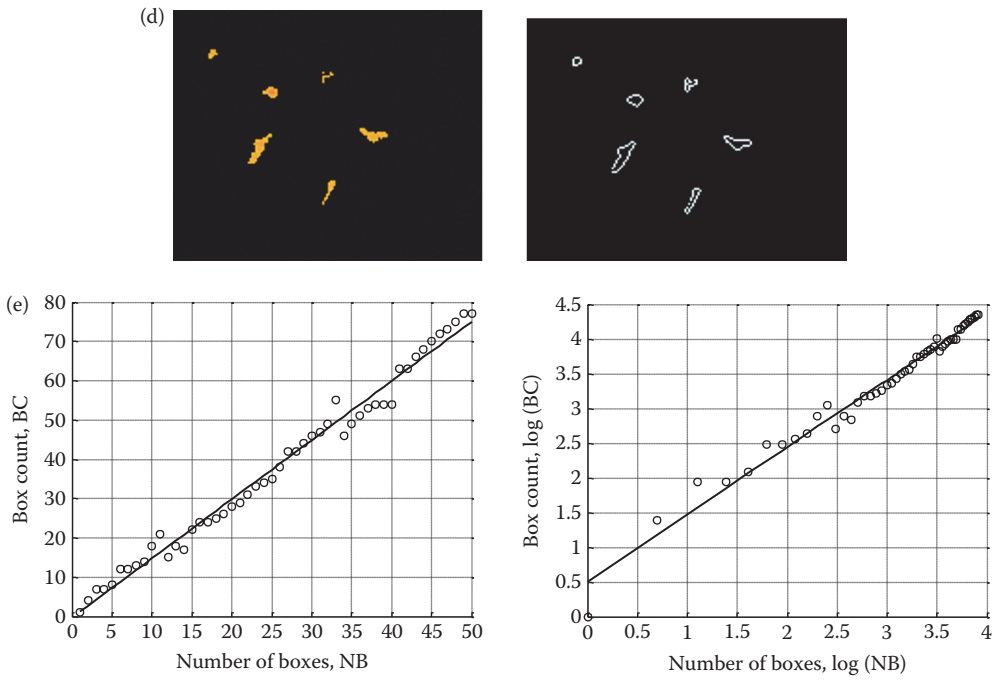

FIGURE 16.5 (continued) (d) B1: (1) The first hottest regions after removing the axilla and close sternal boundaries. (2) Boundaries of part (1). (e) B1: (1) Box count (BC) versus number of boxes (NB). (2) log(BC) versus log (NB).

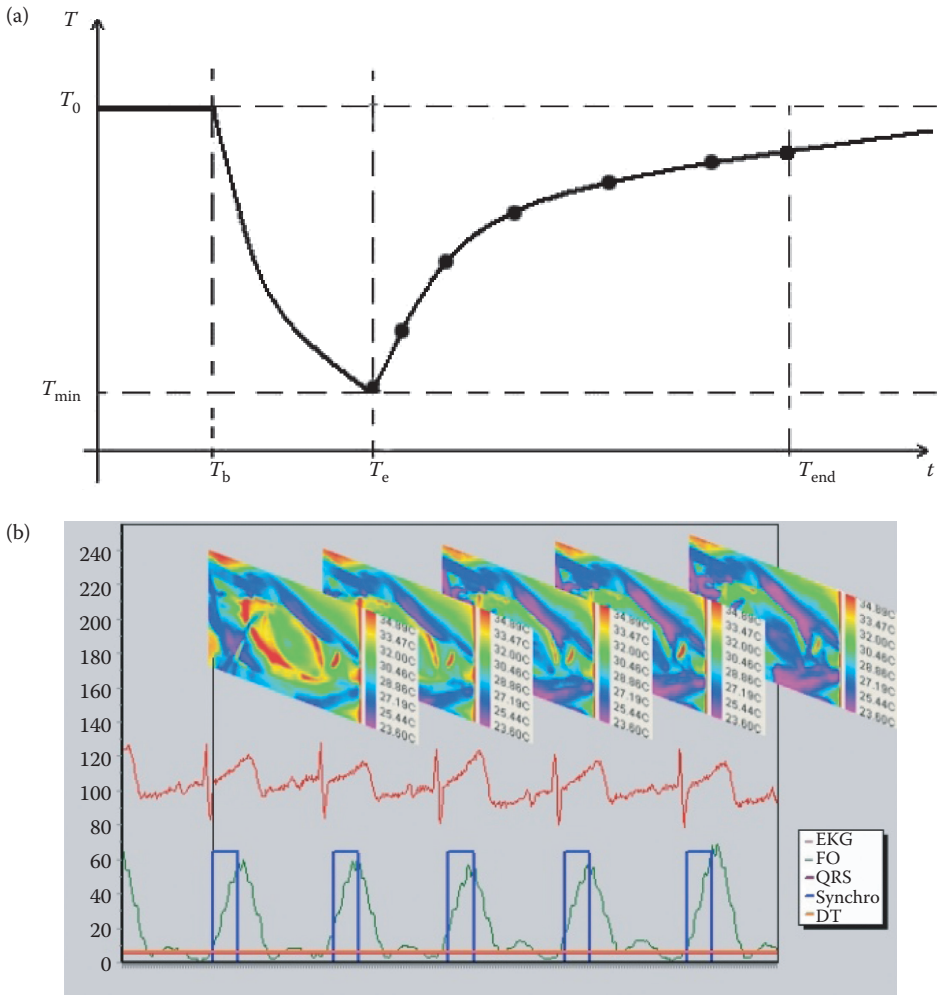

FIGURE 17.4 Measurement procedure requires registration of temperature transients at any pixel *x,y* in time. The example (a) shows the trace of temperature at *x,y*—cooling excitation; $t_{b/e}$—moments at which the cooling source is switched *on* (beginning) and *off* (end of excitation), respectively, t_{end}—time of termination of the recording; dots are indicating moments of thermal image capture; (b) shows that thermal images are measured synchronically with the heart rate, according to QRS.

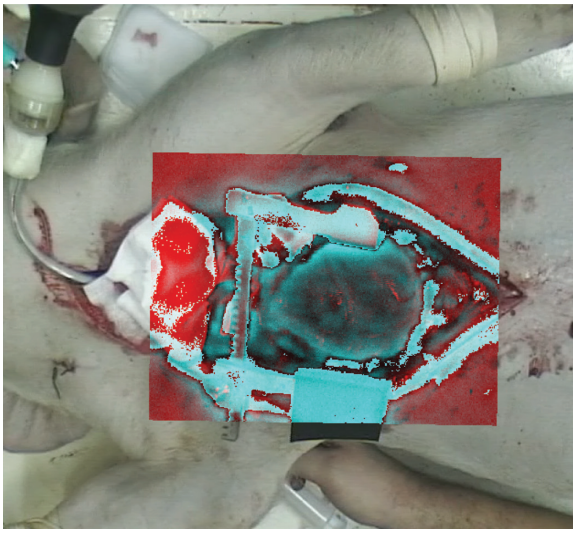

FIGURE 17.5 Matching of visible and IR images may help in recognition of the region of interest.

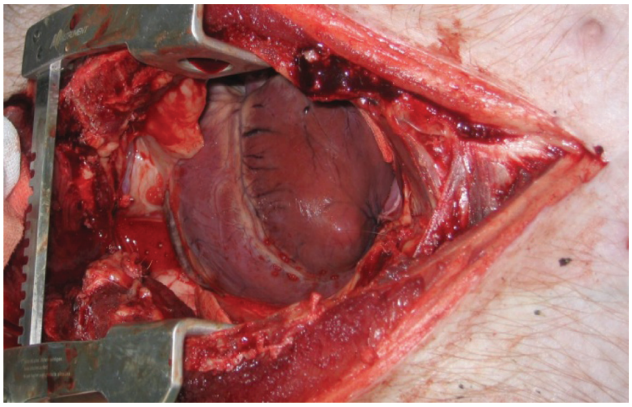

FIGURE 17.7 Exposition of a pig heart before clamping LAD.

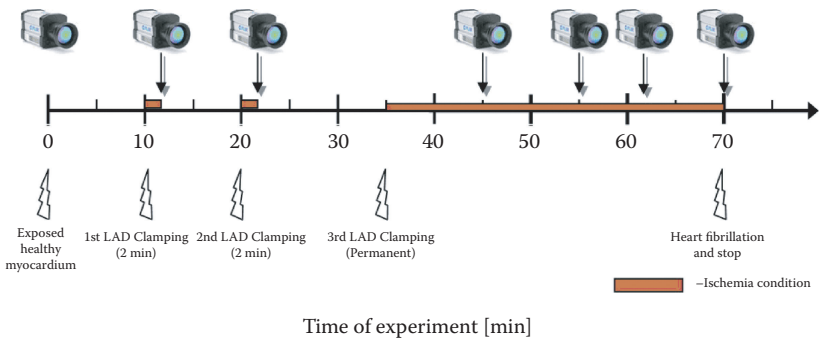

FIGURE 17.9 Experiment schedule with indicated surgery incidents and measurements points; static thermography and ADT as well as electrical impedance measurements.

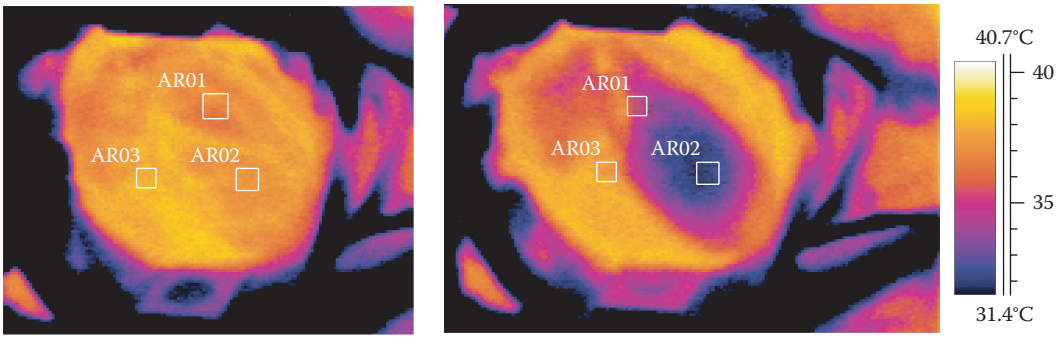

FIGURE 17.10 Thermograms of the myocardium with marked regions of interest AR0x; (a) for normal condition, (b) after clamping of LAD.

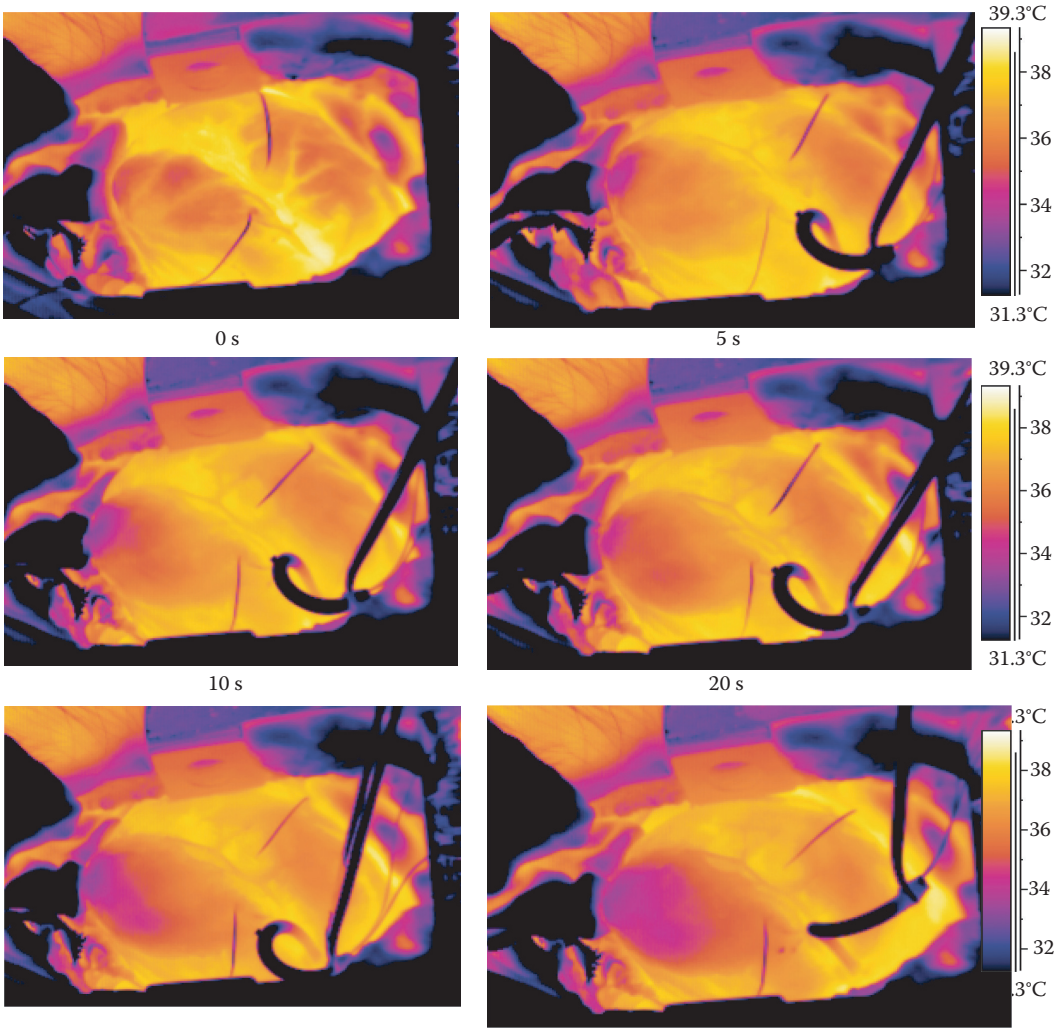

FIGURE 17.13 The static thermograms of the pig heart taken at the indicated times after clamping LAD taken by a camera synchronized with the heart rate. Temperature at the affected region is slowly decreasing; affected vascularization after clamping LAD is evident.

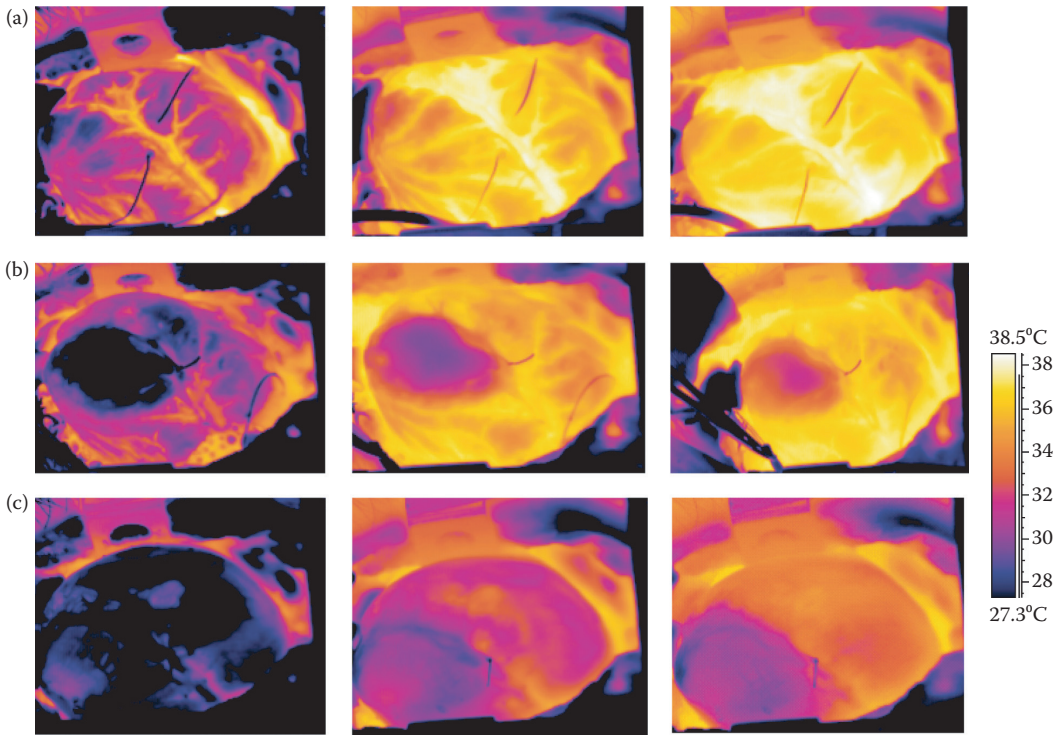

FIGURE 17.14 ADT experiment on the heart during induced heart infarct for different phases of the blood arrest. Thermograms at different moments after stopping cold excitation using CO_2; first column—end of cold excitation, second column—20 s following stopping of cold excitation, third column—90 s following stopping of cold excitation, rows: (a) examination of a healthy heart (before clamping LAD according to Figure 17.9); (b) 40 min after stopping blood flow in LAD, (c) 80 min after blood arrest.

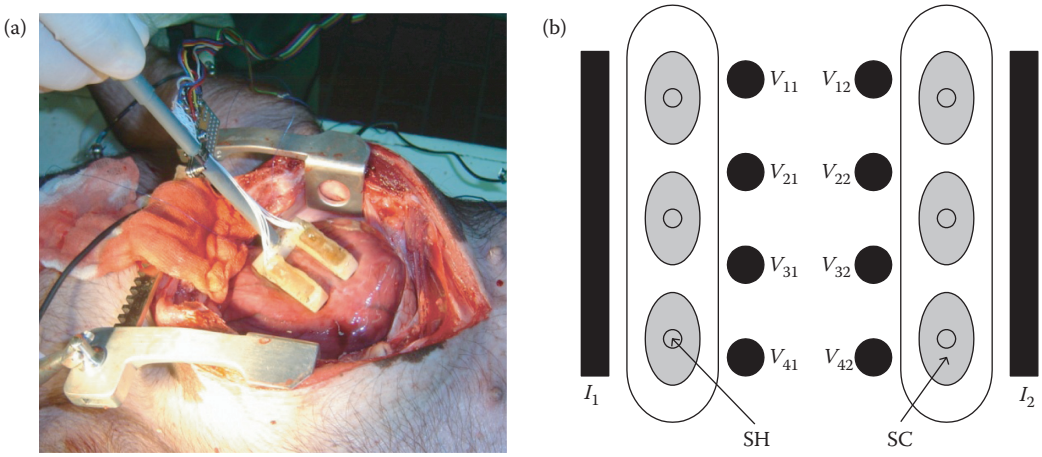

FIGURE 17.16 (a) Mechanical stabilizer with electroimpedance electrodes applied to the heart muscle; (b) the schematic diagram (bottom view) of the probe combined with sucking holder; I and V stand for current and voltage electrodes while SH and SC mark sucking holes and cups, respectively.

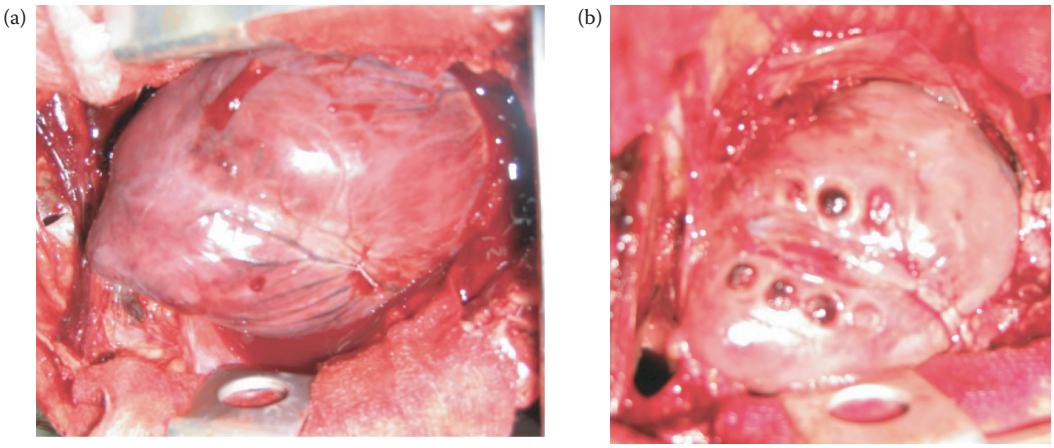

FIGURE 17.17 (a) The pig heart before application of the stabilizer; (b) after intervention—the hematoma visible at the positions of the sucking chambers.

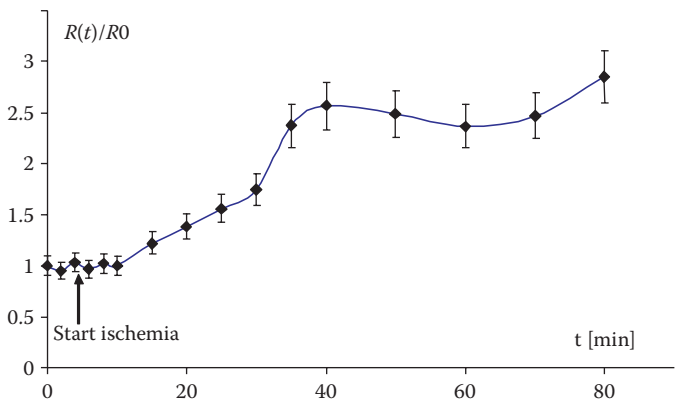

FIGURE 17.18 Resistivity measured at 5 kHz for the set of electrodes in Figure 17.16 (I_1, I_2, V_{21}, and V_{22}) and the mechanical stabilizer placed close to the center of the affected vascularization region of the heart muscle.

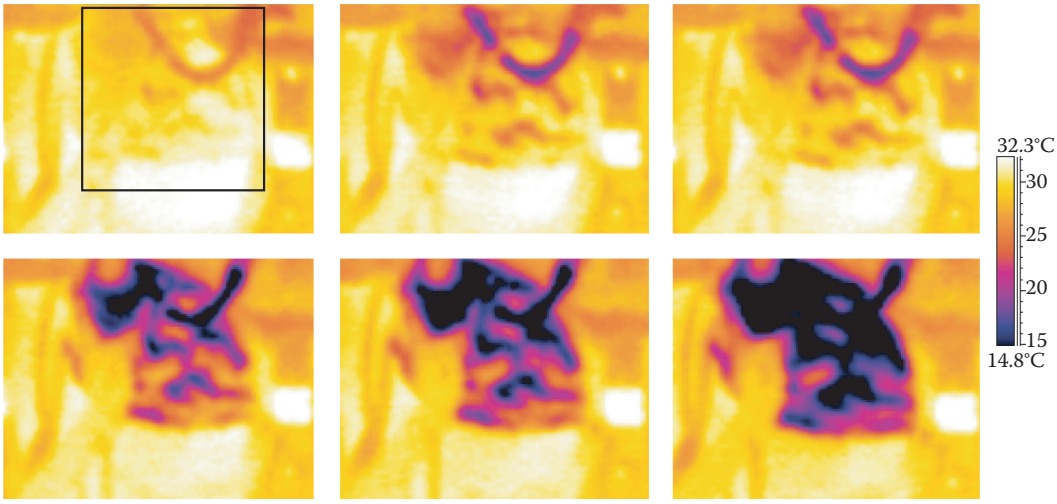

FIGURE 17.19 Series of thermograms during antegrade cardioplegia taken every 10 s; one can see a progressive decrease of the heart muscle temperature; position indicated by the rectangle.

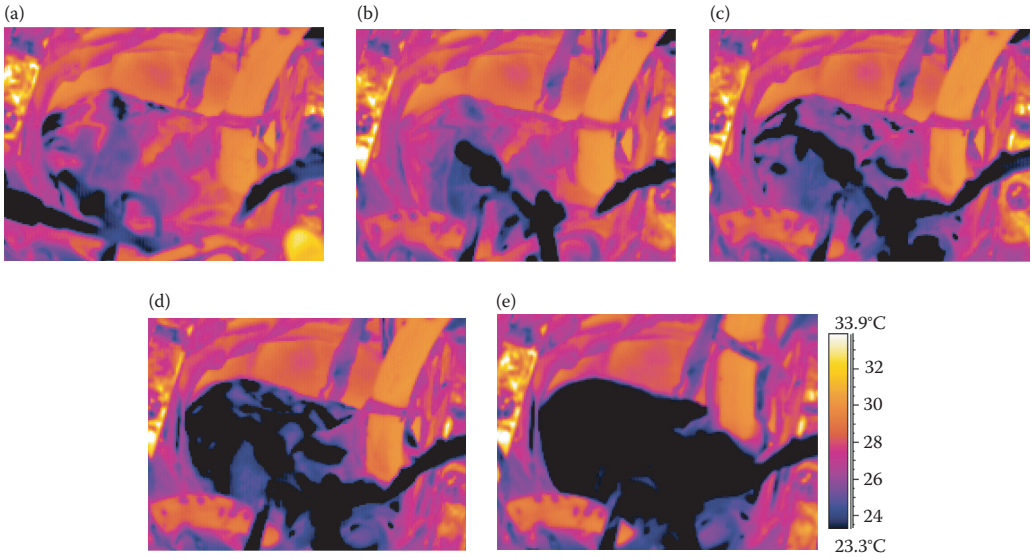

FIGURE 17.20 Series of thermograms during cardioplegia (retro/ante); (a) application of 500 mL of cardioplegia liquid retrograde; (b) continuation using antegrade cardioplegia at 10 s after beginning of antegrade, (c) 25 s, (d) 45 s, (e) 75 s.

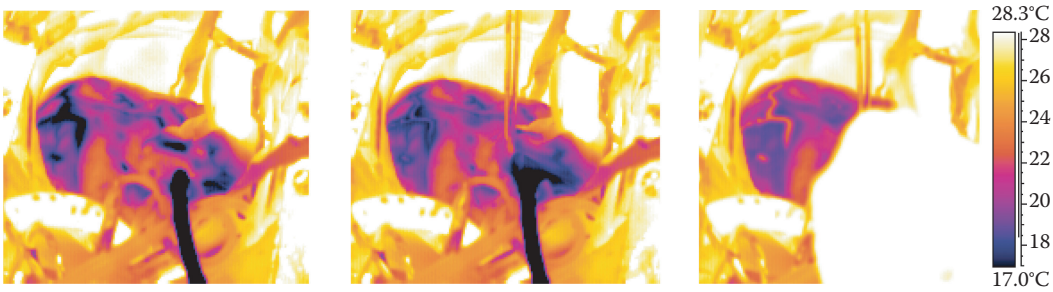

FIGURE 17.21 (a) Thermogram after stopping cardioplegia and respectively (b) after 3 s and (c) after 13 s; the arrow shows LAD.

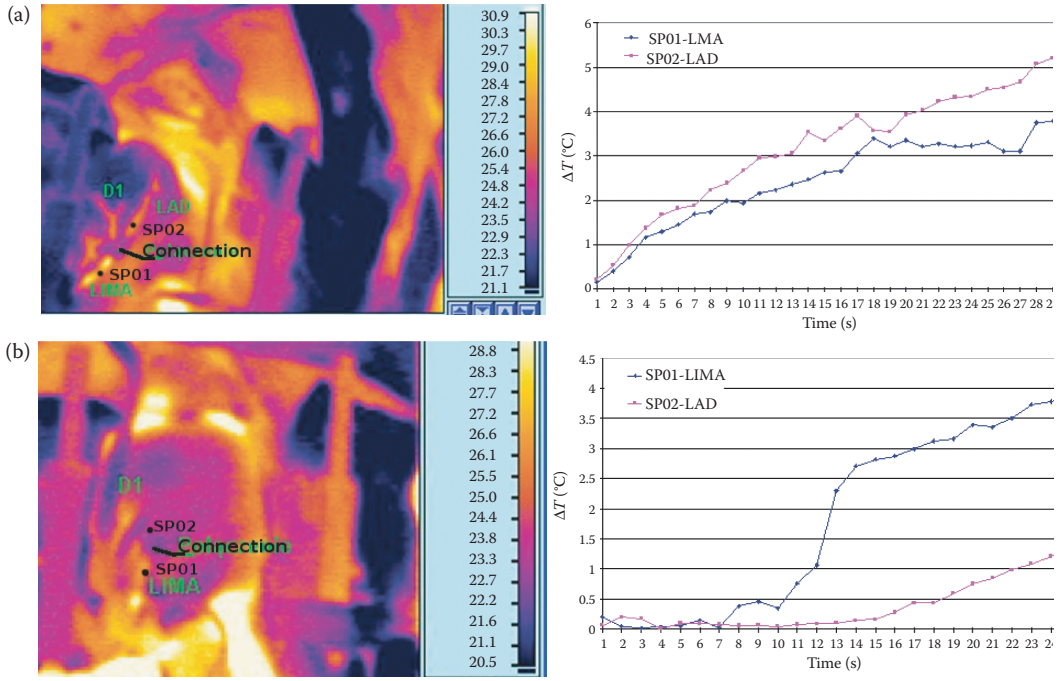

FIGURE 17.22 Quantitative analysis of the graft LIMA-LAD; (a) correct case with temperatures rising in time at the points SP01 and SP02; (b) nonfunctioning graft at SP02—lack or affected rise of temperature in LAD.

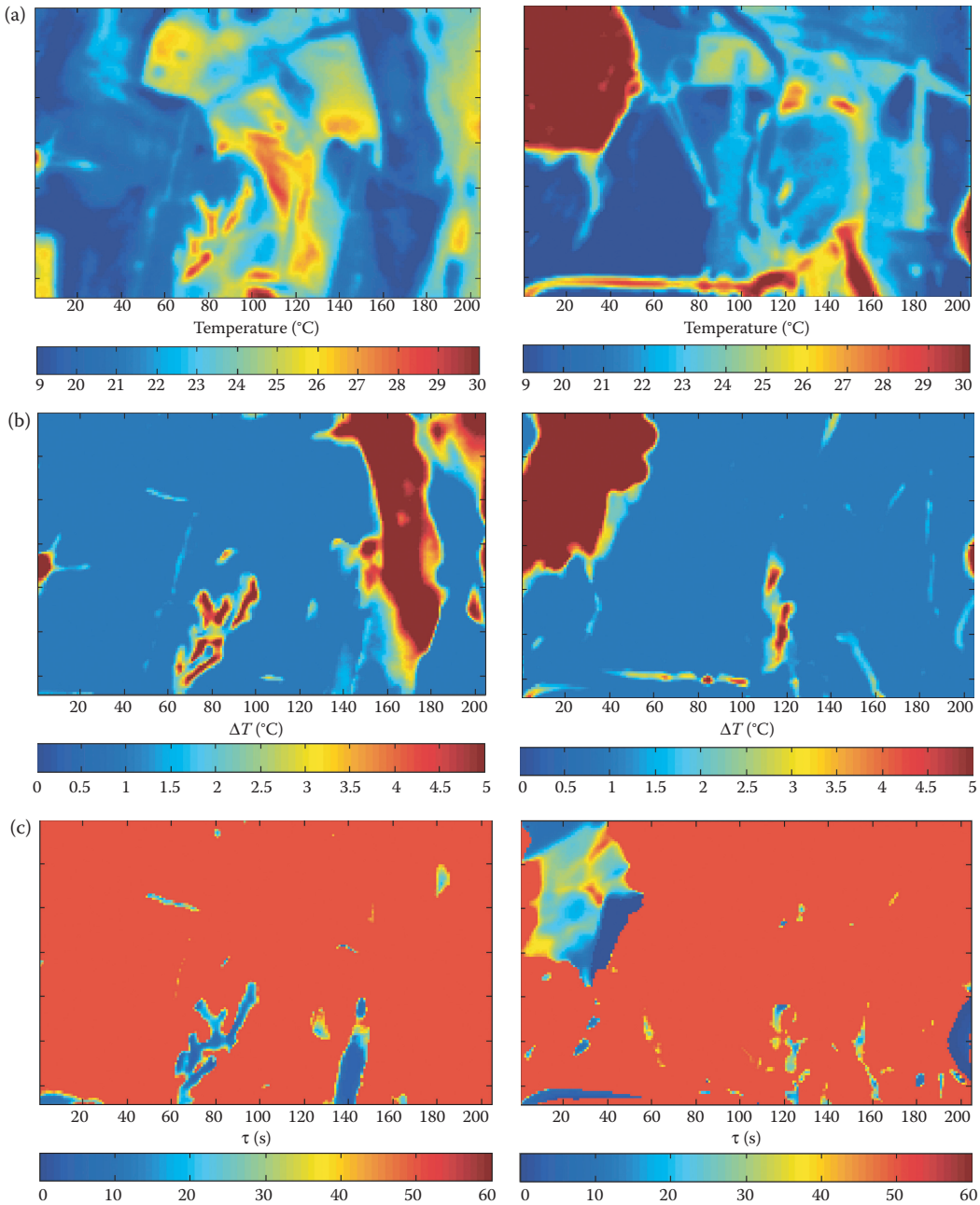

FIGURE 17.23 Correct (left column) and requiring reoperation (right column) LIMA-LAD grafts; (a) thermal images at 20 s after unclamping the graft; (b) recorded rise of temperature; (c) time constants according to the model (4).

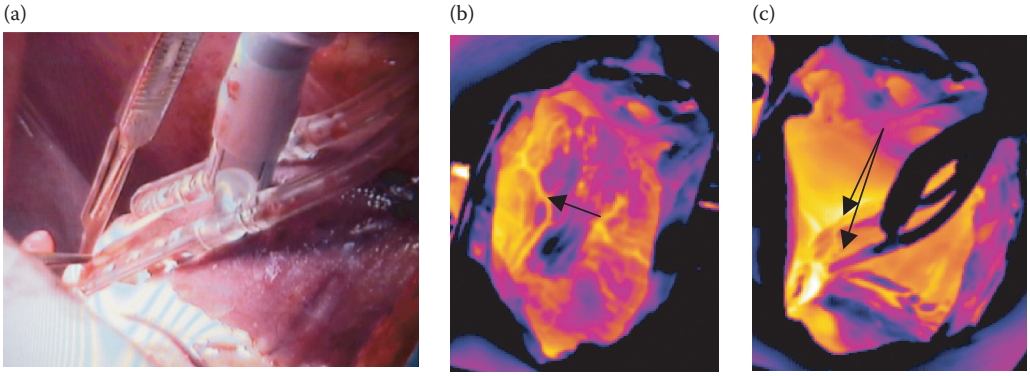

FIGURE 17.24 OP CABG intervention: (a) view of the mechanical heart stabilizer, (b) thermogram showing blockade at the LAD (see arrow), (c) myocardium under LAD with the stabilizer arms sucked to hold it in a stable position (see arrows).

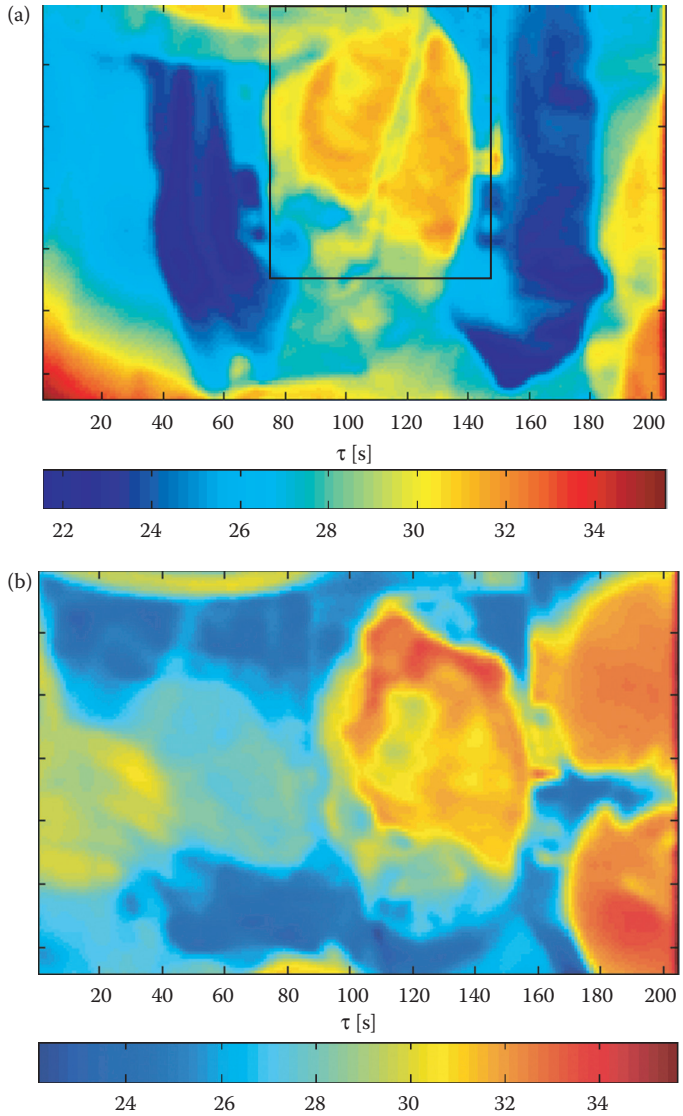

FIGURE 17.25 Perfusion of myocardium (a) before and (b) after CABG; the heart region is indicated by a rectangle.

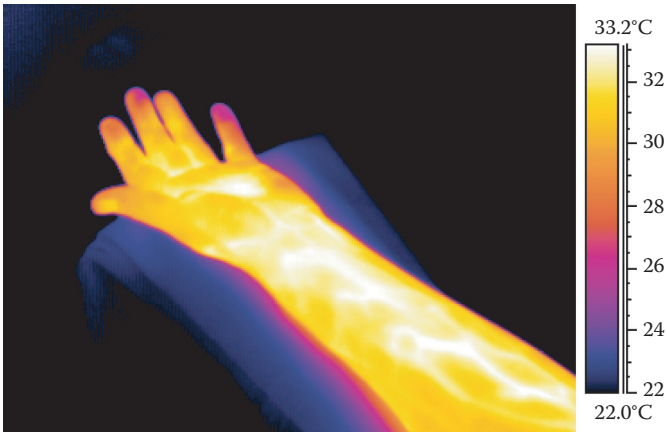

FIGURE 17.26 Vascularization of a hand after mechanical exercise before extracting the radial artery for a bypass. This is a reference image for further analysis of hand function recovery after reconvalescence lasting typically 3 months.

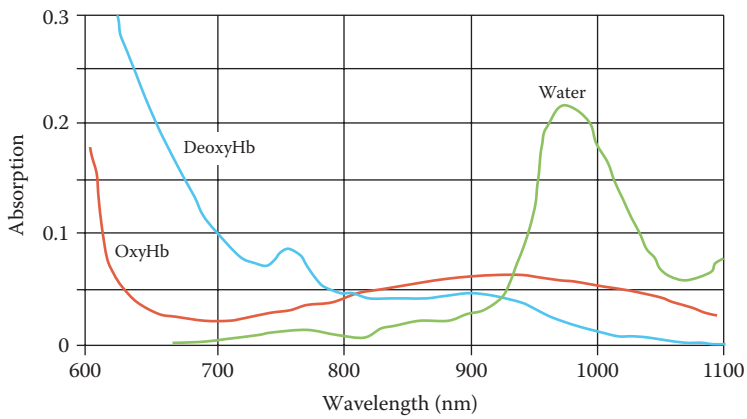

FIGURE 19.1 Absorption spectra of the three major components of tissue in the NIR region: oxy- and deoxyhemoglobin, and water.

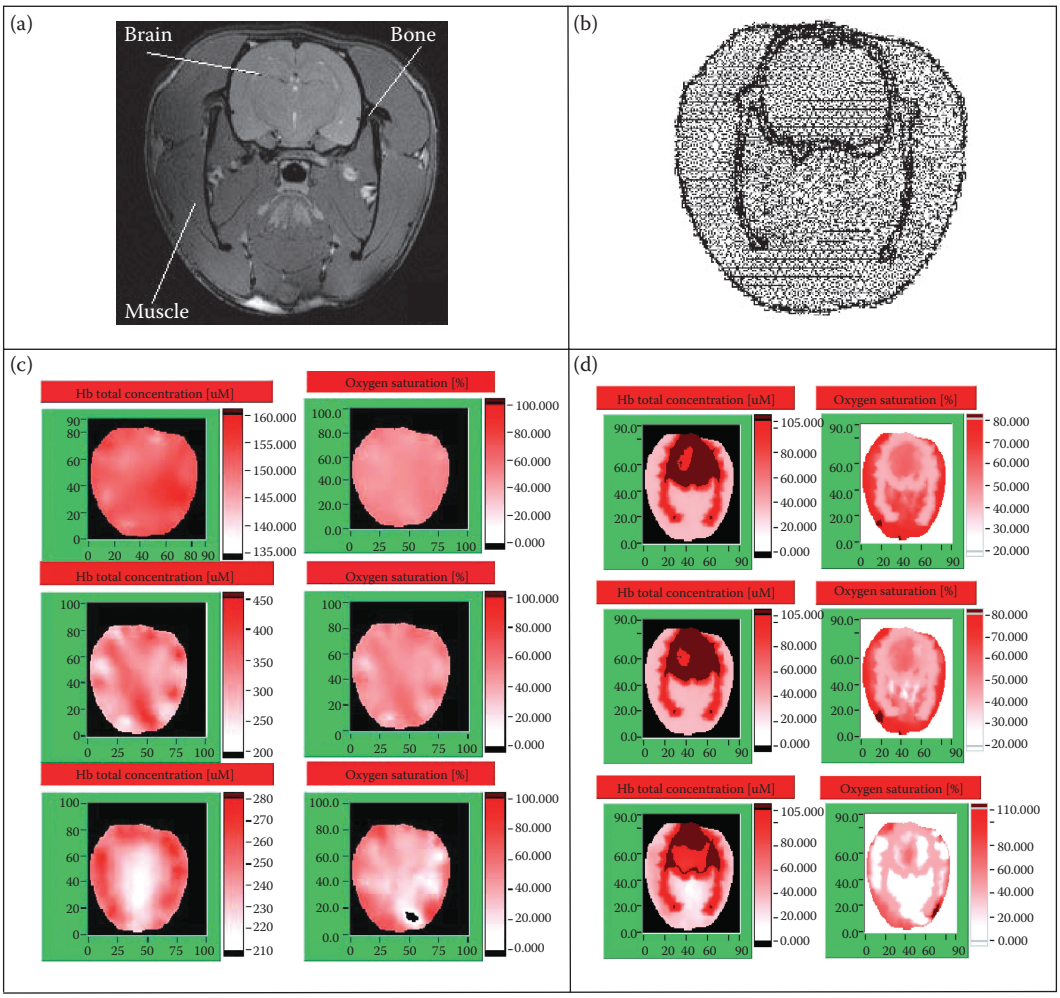

FIGURE 19.2 Functional imaging of rat cranium during changes in inhaled oxygen concentration. (a) MRI image; (b) creation of the mesh to distinguish different compartments in the brain; (c) map of hemoglobin concentration and oxygen saturation of the rat brain without structural constraints from MRI; (d) same as (c) with structural constraints, including tissue heterogeneity. In (c) and (d), the rows from top correspond to 13%, 8%, and 0% (after death) oxygen inhaled. (Courtesy of Dartmouth College.)

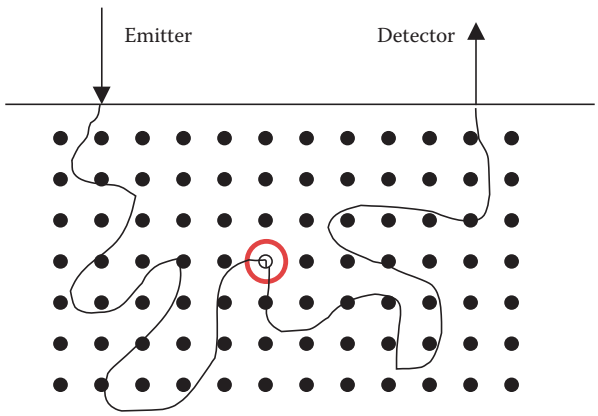

FIGURE 19.3 2D random walk lattice showing representative photon paths from an emitter to a specific site and then to a detector.

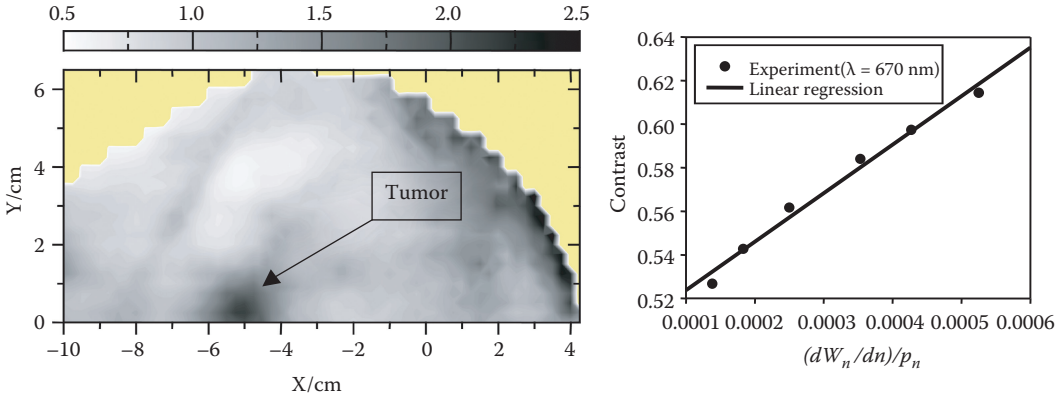

FIGURE 19.5 (a) 2-D optical image of the breast with the tumor. (Courtesy of Physikalich.-Techniche-Bundesanstalt, Berlin.) (b) Contrast obtained from linear scan through the tumor plotted versus the derivative of PSF. From the linear regression, the scattering coefficient of the tumor is deduced.

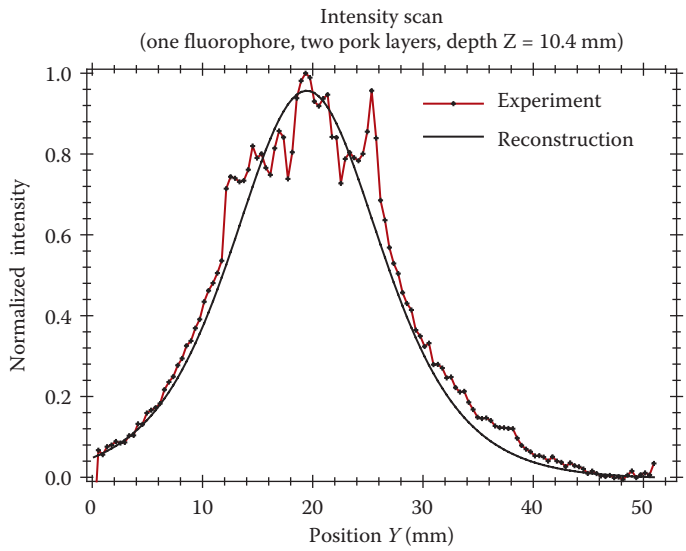

FIGURE 19.6 Intensity scan of a fluorophore 10.4 mm below the tissue surface.

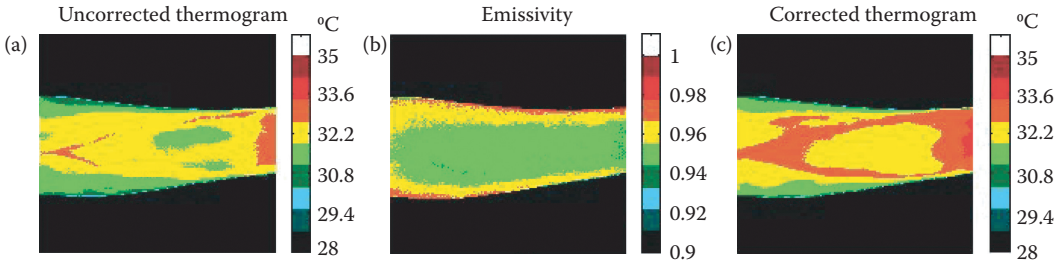

FIGURE 19.8 An example of images obtained from the forearm of a normal healthy male subject. (a) Original thermogram; (b) emissivity image; and (c) thermogram corrected by emissivity.

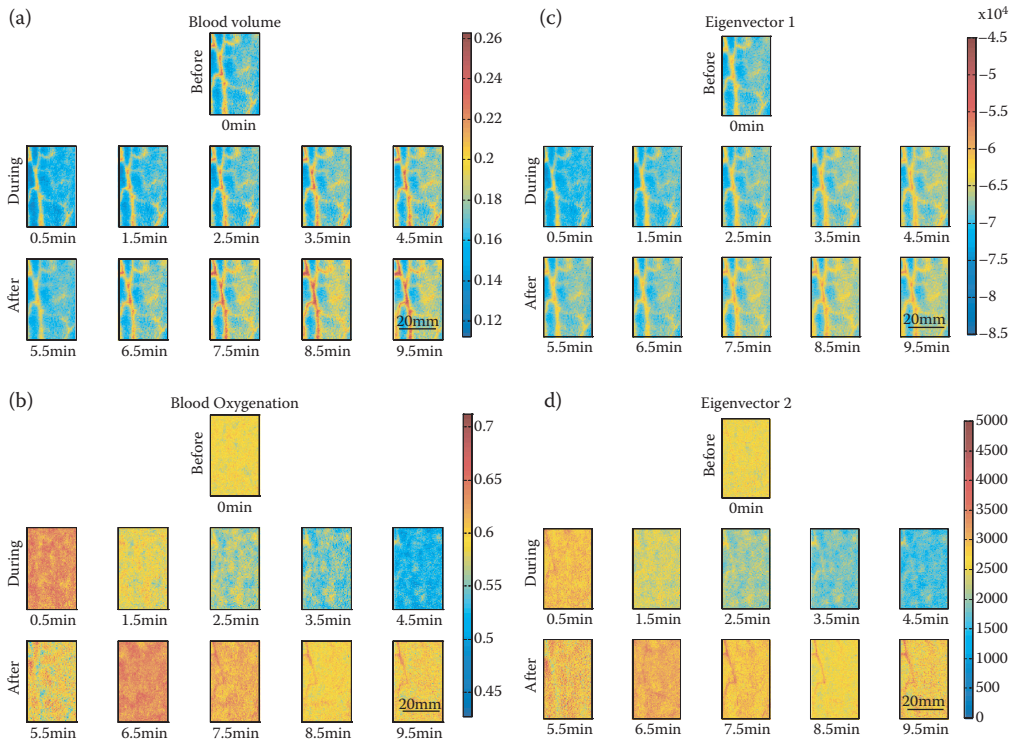

FIGURE 19.10 Typical multispectral results from a healthy volunteer's forearm. Reconstructed fractional blood volume (a) and blood oxygenation (b) over time. Principal component analysis results with eigenvector 1 (c) and eigenvector 2 (d). (From J. Kainerstorfer, M. Ehler, F. Amyot et al., *J. Biomed. Opt.*, 15, 2010. With permission.)

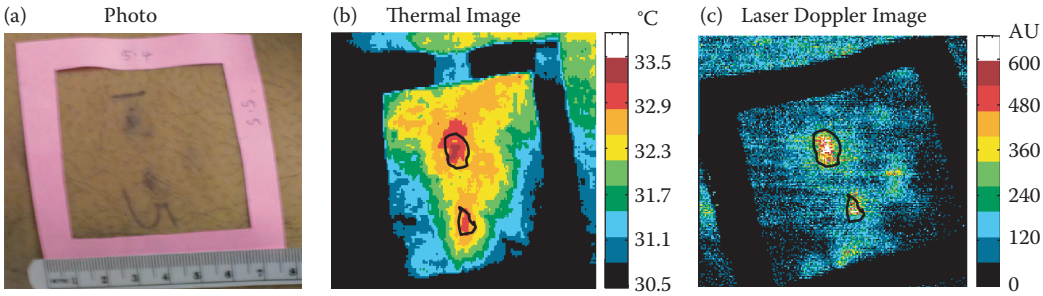

FIGURE 19.11 Typical multimodality images obtained from a patient with KS lesion. The numbers "1" and "5" in the visual image were written on the skin to identify the lesions for tumor measurement. The solid line in the thermal and LDI demarks the border of the visible KS lesion. Shown is a representative patient from the study reported in Ref. [111].

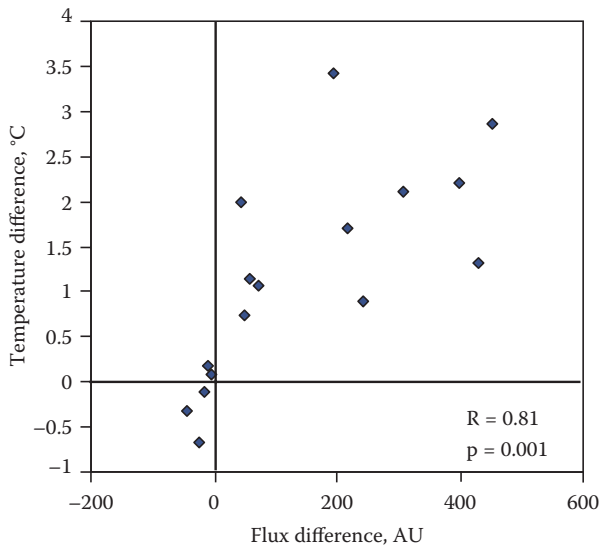

FIGURE 19.12 Relationship between the difference in temperature and flux assessed by LDI of the lesion and surrounding area of the lesion of each subject. A positive correlation was observed between these two methods ($R = 0.8$, $p < 0.001$). (From M. Hassan, R. F. Little, A. Vogel et al., *TCRT*, 3, 451–457, 2004. With permission.)

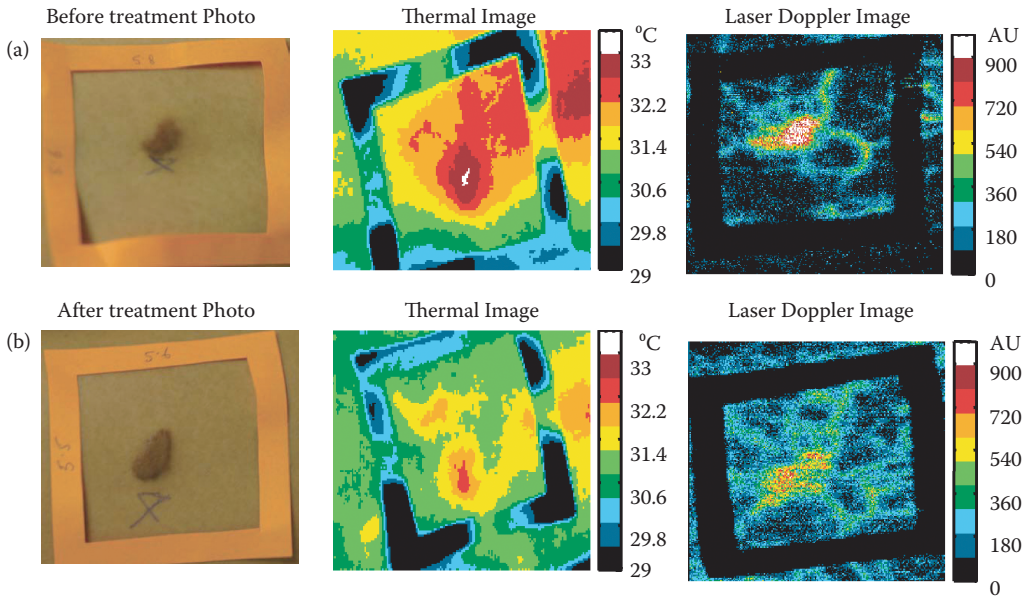

FIGURE 19.13 Typical example of lesion obtained from a subject with KS (a) before and (b) after the treatment. Improvement after the treatment can be assessed by the thermal or LDI images after 18 weeks. Shown is a patient from the clinical trial reported in Ref. [111].

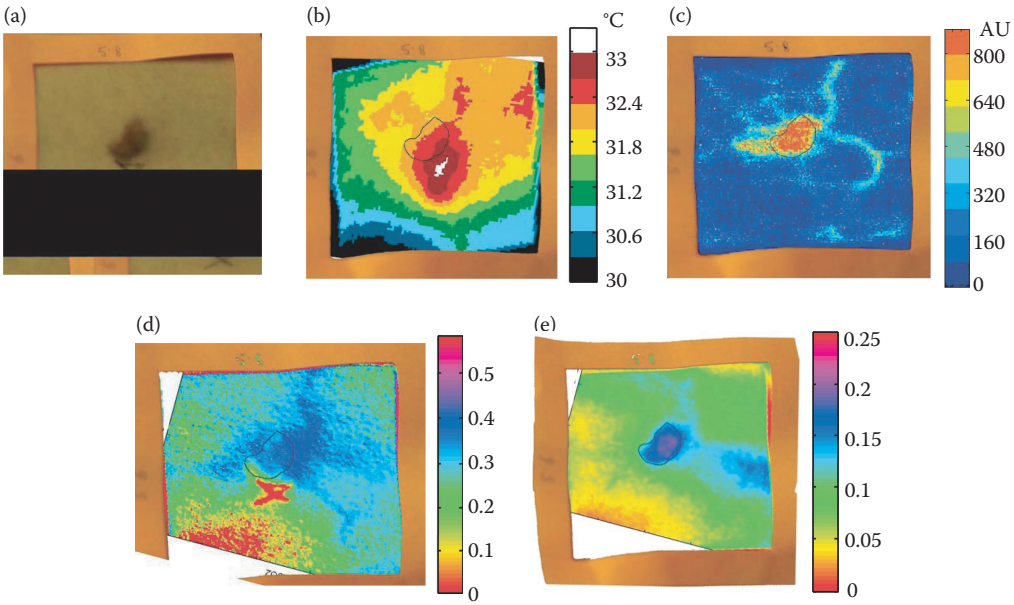

FIGURE 19.14 Set of comparative images of a KS patient. Visual, thermal, laser Doppler, HbO_2 fraction, and tissue blood volume fraction images are provided. (From A. Vogel, M. Hassan, F. Amyot et al., *Biomedical Optics 2006*, *Technical Digest*, p. SG2, 2006.)

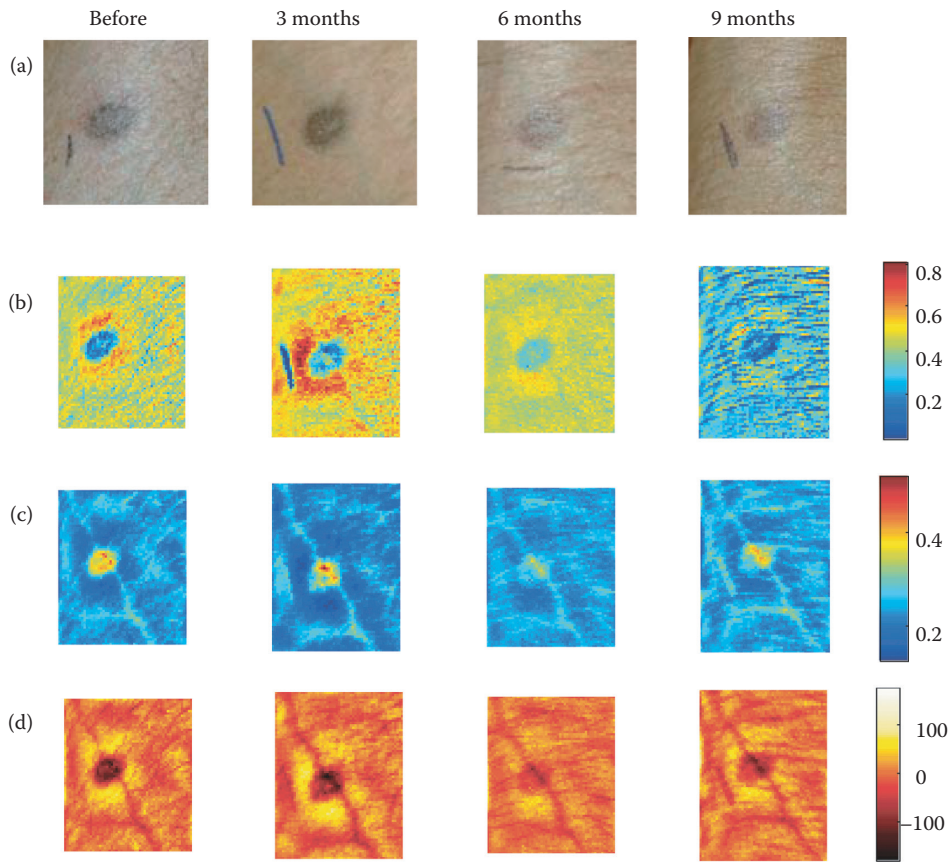

FIGURE 19.15 Digital images of KS lesion over time. Left to right: week 0, 14, 26, and 38 (a); blood oxygenation over time (b); blood volume over time (c); projection along the first principal component (d). (From Kainerstorfer, J. M., F. Amyot, M. Hassan et al., *Biomedical Optics, OSA Technical Digest*, p. BME6, 2010. With permission.)

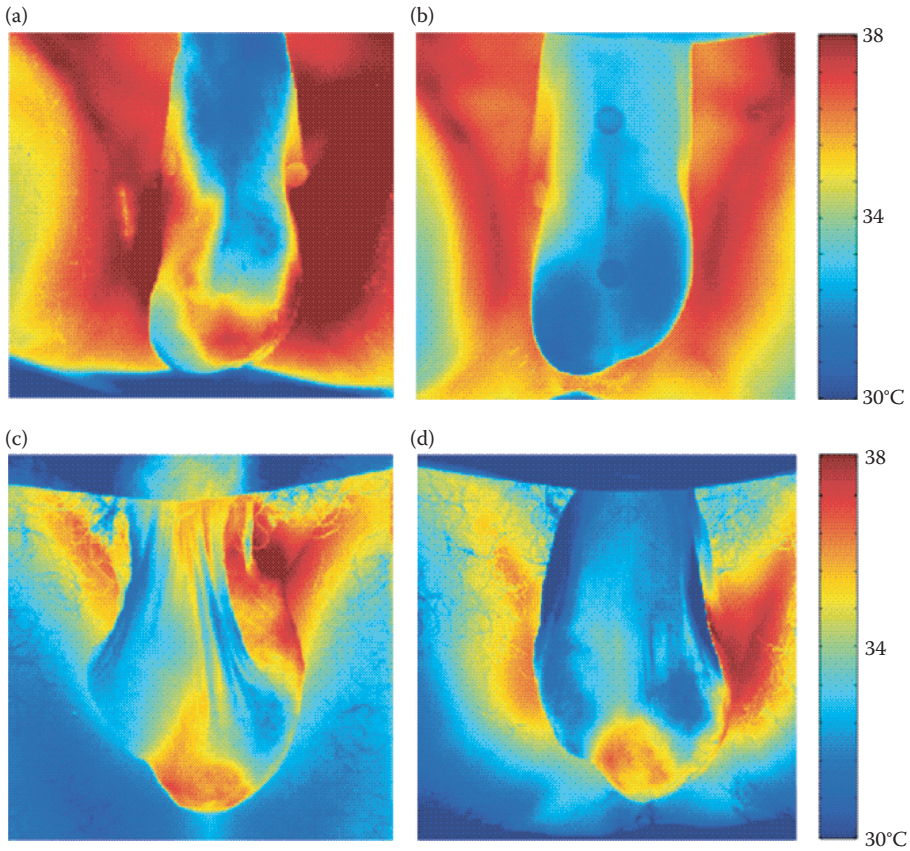

FIGURE 20.1 (a) Second-grade right varicocele. The temperature distribution all over the scrotum clearly highlights significant differences between affected and unaffected testicles. (b) The same scrotum after varicocelectomy. The surgical treatment reduced the increased temperature on the affected hemiscrotum and restored the symmetry in the scrotal temperature distribution. (c) Third-grade left varicocele. (d) The same scrotum after varicocelectomy. The treatment was unsuccessful in repairing the venous reflux, as documented by the persisting asymmetric scrotal distribution.

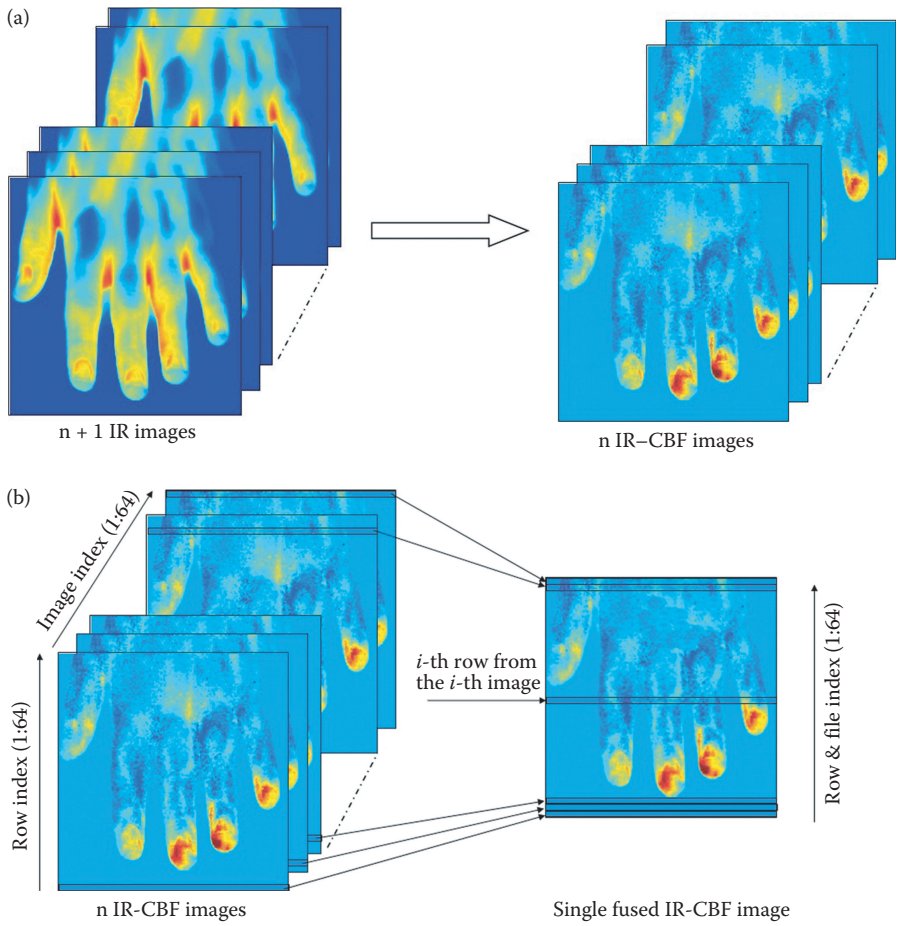

FIGURE 20.5 From the thermal IR images series to the IR-CBF image. (a) The series of $n + 1$ IR images is converted into a series of n IR-CBF images by applying the proposed bio-heat model. (b) The series of n IR-CBF images is then condensed in a single IR-CBF image. Each i-th row of the IR-CBF image is obtained by pasting the i-th row ($i = 1{:}64$) of the i-th image ($i = 1{:}64$) of the IR-CBF image series. In this way, each row out of the 64 ones of the final and single IR-CBF image is synchronous with the corresponding row out of the 64 ones in the LDI-IR image.

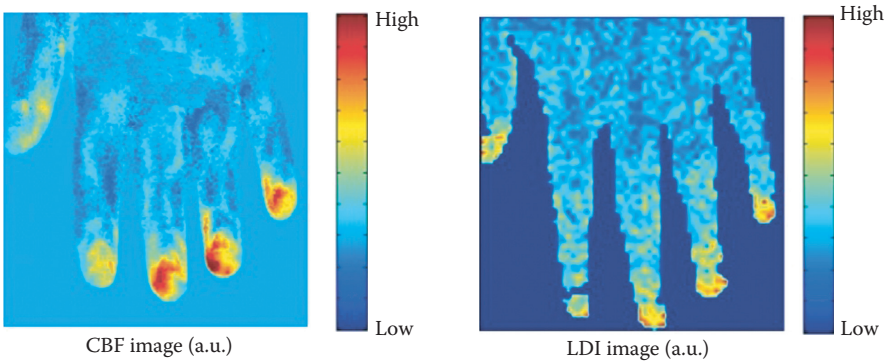

FIGURE 20.6 CBF images (in arbitrary units) obtained with the proposed method (upper panel, IR-CBF) and recorded with LDI imager (lower panel). Color bar reports false-color visualization of the perfusion distribution. The overall distributions appear to be consistent, both images similarly showing the same high-perfusion and low-perfusion regions.

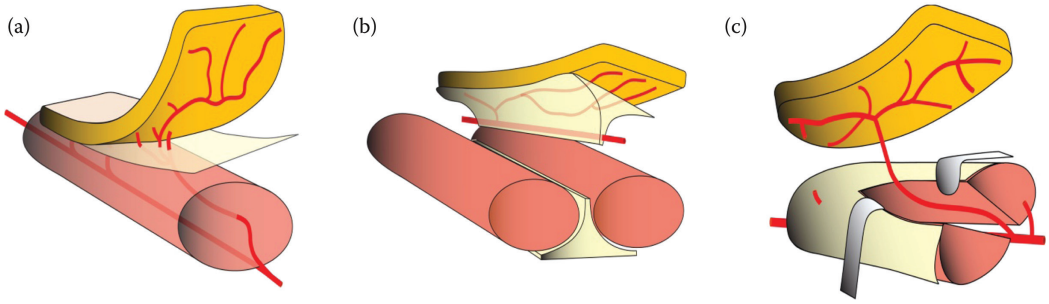

FIGURE 28.1 The evolution from myocutaneous flap (a) to fasciocutaneous flap (b) to perforator flap (c). With the perforator flap, no muscle or fascia is included. In (c), the perforator flap receives its blood supply from a perforator that passes through the muscle and emerges from the source vessel that lies underneath the muscle.

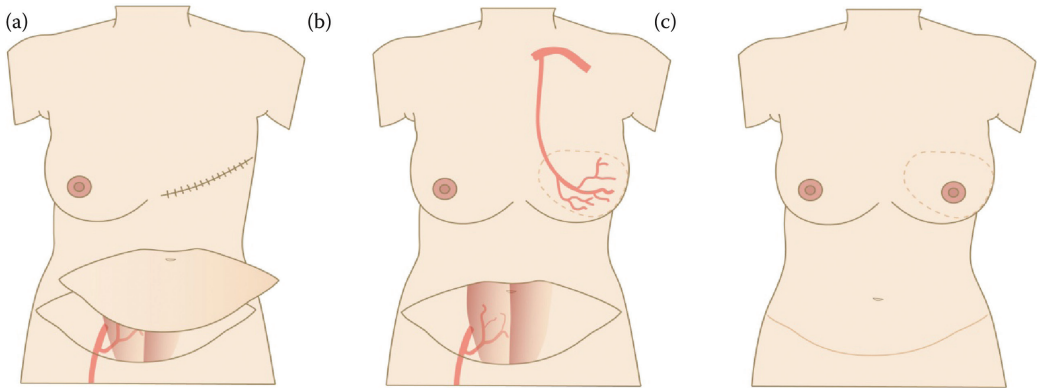

FIGURE 28.2 Breast reconstruction with a DIEP flap. (a) The abdominoplasty flap is harvested from the lower abdomen as a DIEP flap, based on one perforator from the deep inferior epigastric artery and vein. (b) After the flap is transferred to the thoracic wall, its vessels are anastomosed to the internal mammary vessels. (c) A breast is reconstructed and the lower abdomen is closed as an abdominoplasty.

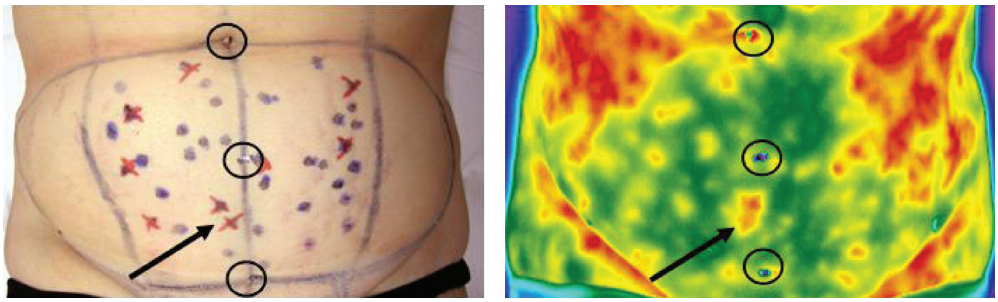

FIGURE 28.3 Left: This photograph of the lower abdomen shows the locations where arterial Doppler sounds were heard and marked with blue dots. Some of the blue spots are marked with red crosses. These arterial Doppler sounds were associated with hot spots seen in the thermal images shown on the right. The arrows indicate the location where a loud arterial Doppler sound was heard and was associated with a bright hot spot. This perforator could be used to supply a DIEP flap. The circles indicate the positions of small pieces of metal tape used as reference markers.

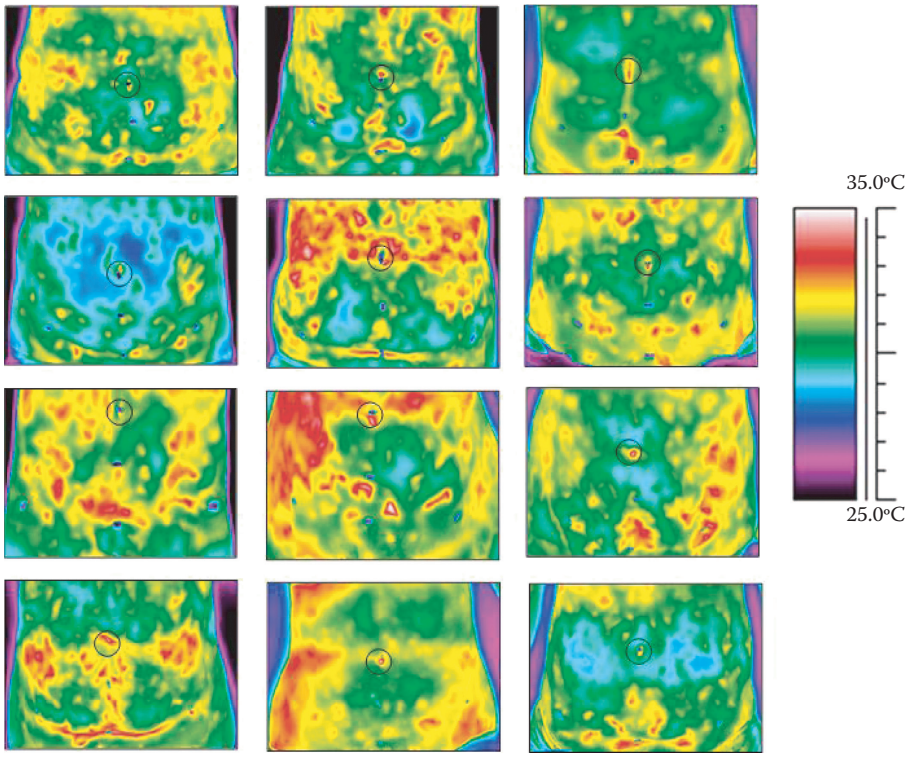

FIGURE 28.4 Preoperative infrared thermal images of the abdominal area of 12 female patients indicating thermal asymmetry. The black circle in each image indicates the position of the navel. The figure illustrates the large variability in the distribution and intensity of hot spots, not only between the left and right side of each individual patient but also between patients.

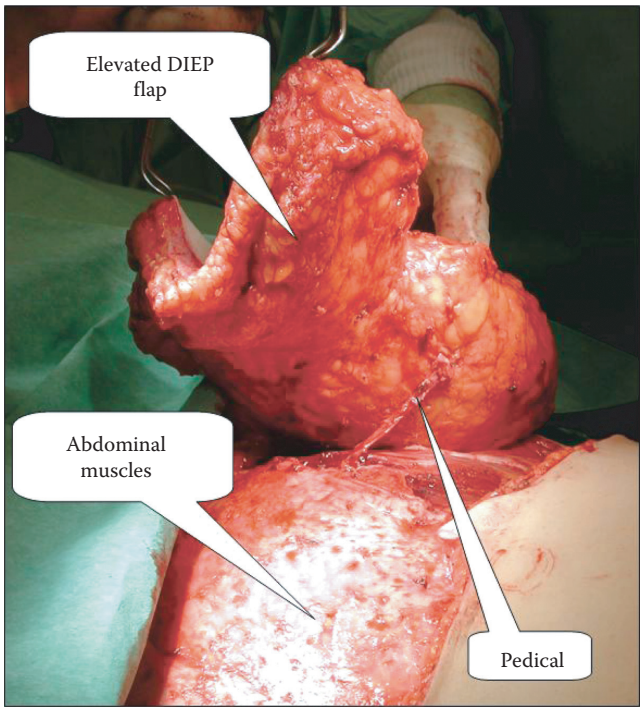

FIGURE 28.5 The skin and subcutaneous tissue of the lower abdomen is elevated as a DIEP flap. The image was taken just prior to transfer of the flap to the thoracic area. The flap receives its blood supply via the pedicle which is the perforator and consists of one artery and one vein. Note no muscle is included.

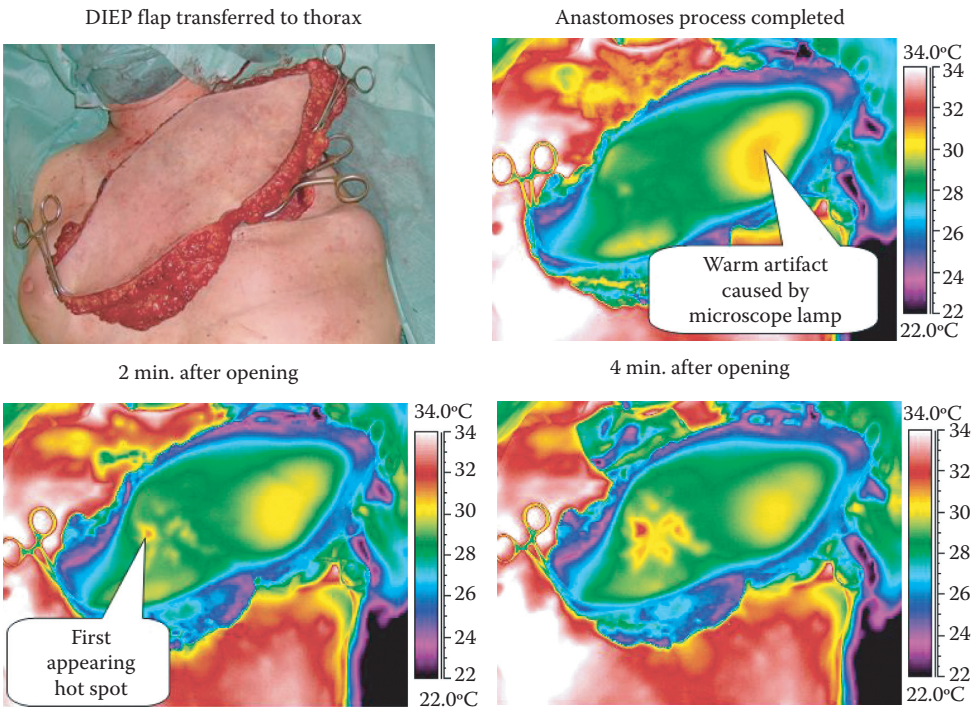

FIGURE 28.6 Digital photograph of a free DIEP flap. The infrared thermal images demonstrate a rewarming of a free DIEP flap after completion of a successful microsurgical anastomosis. The anastomosis was opened in the upper right image. The other images were taken at 2 min intervals after the anastomosis had been opened and the blood flow to the flap was restored. Note the appearance of hot spots that rapidly increase in size and number. A thermal artifact (diffuse warm area) can be seen in the upper left thermal image caused by heating from the microscope lamp. This area cools down after removal of the heat source.

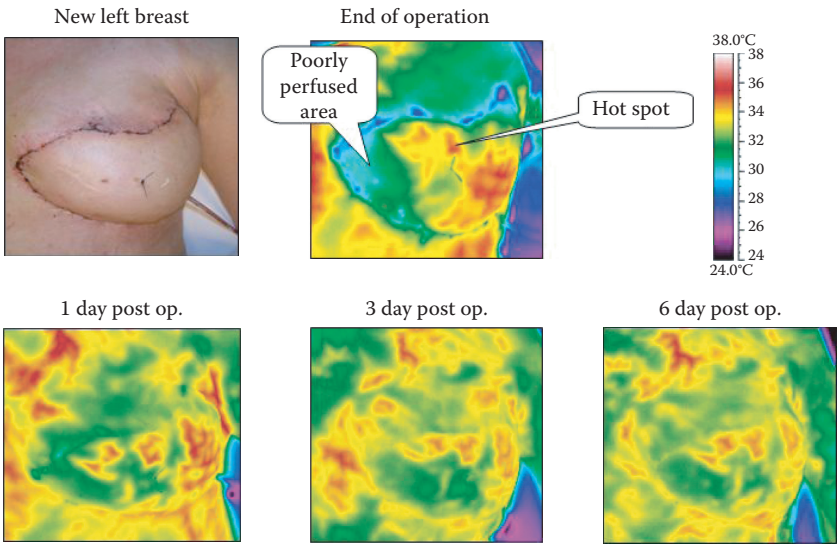

FIGURE 28.7 The photograph on the top left shows a newly reconstructed left breast with a DIEP flap. The infrared thermal images show an improved perfusion over time. Not that part of the newly reconstructed breast is less well perfused at end of operation (indicated by a cooler area) but improves in the days as indicated by the appearance of new hot spots.

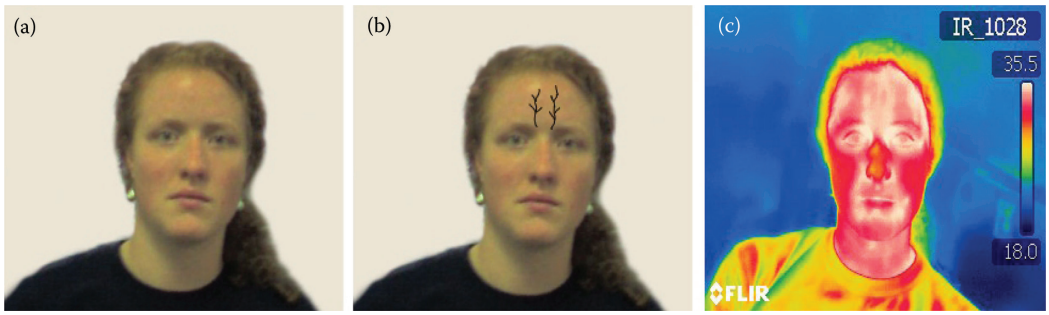

FIGURE 28.8 (a) Digital picture of forehead. (b) The supratrochlear arteries can be localized by clinical landmarks and are typically found originating near the inferior glabellar creases. These near parallel vessels run vertically approximately 1.5–2.0 cm from the midline forehead. (c) Infrared image of forehead.

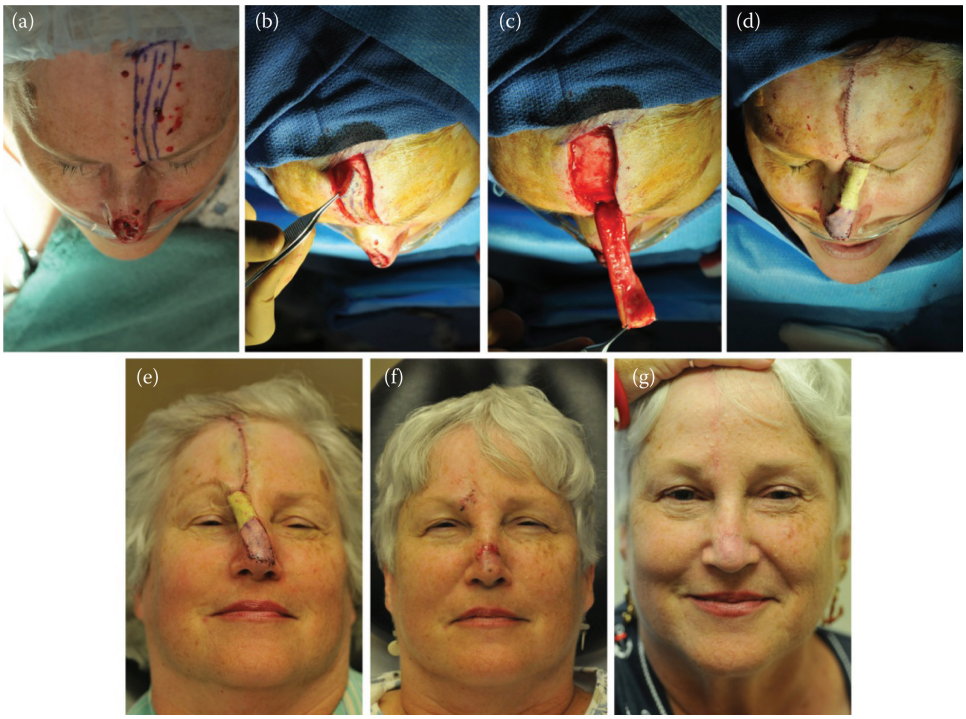

FIGURE 28.9 Paramedian forehead flap reconstruction of a surgical defect following Mohs micrographic surgery for a basal cell carcinoma. The interpolation flap is based on the right supratrochlear artery (a). The flap is elevated superficially at the distal aspect and at the level of the periosteum at the proximal aspect (b, c) to ensure patency of the supratrochlear artery. The flap is subsequently rotated on its proximal base into position to accommodate the surgical defect where it remains for 2–3 weeks (d, e). The second stage of the reconstruction involves taking the flap down (f). The final reconstruction (g) offers a cosmetically acceptable reconstruction.

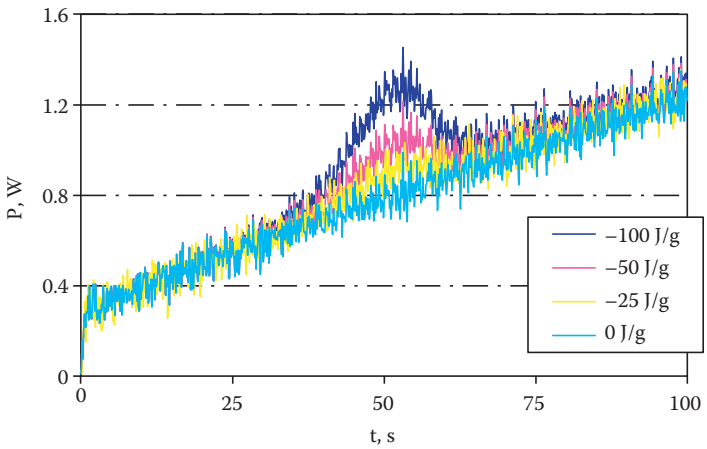

FIGURE 30.5 Temporal behavior of laser power as a function of enthalpy of tentative first-order reaction with Arrhenius-type reaction rate being constant during heating of the local area of the sample with a constant rate 1°C/s. The laser beam has Gaussian intensity distribution $W_L = 4$ mm; $\chi = 0.125$ mm^2/s; $\rho C_p = 3.5$ J cm^3/°C; $\alpha = 10$ cm^{-1}.

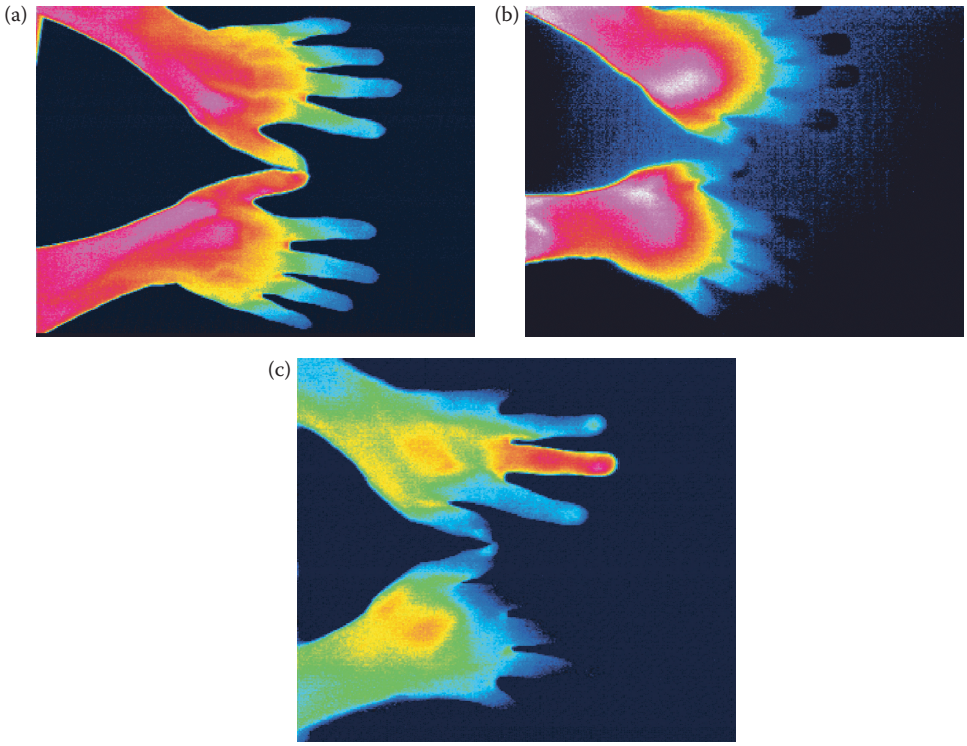

FIGURE 33.2 Thermal hand images of healthy subject (left and middle) together with a thermogram showing an inflammation (right).

FIGURE 33.5 Global visualization view of complete thermal image database.

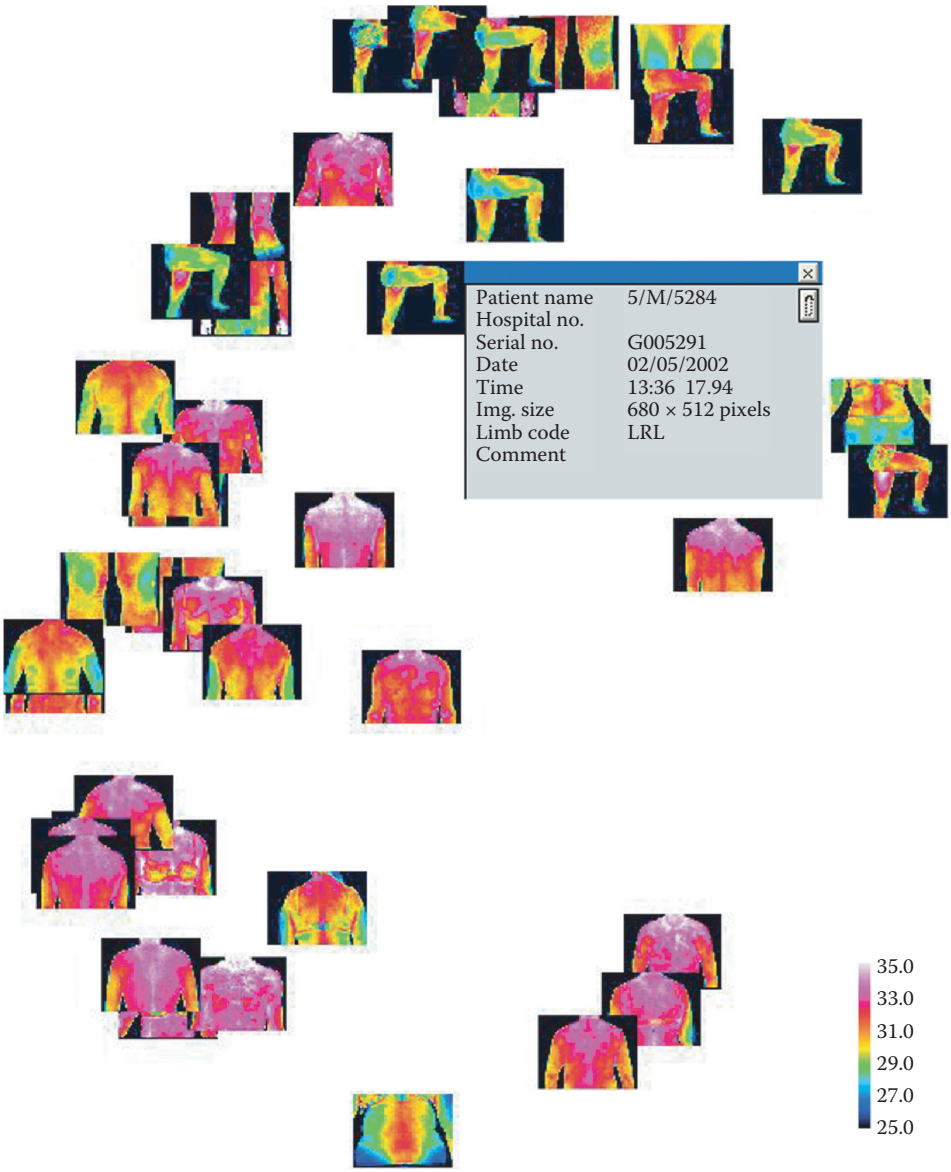

FIGURE 33.6 Zoomed-in area showing leg and upper body images.